

Department of
Physics and Astronomy
University of Heidelberg

Bachelor thesis
in Physics
submitted by
Grischa M. Klimpki
born in Hamburg
May 2012

***Towards in-vivo Ion Range
Measurements using Fluorescent
Nuclear Track Detectors***

This Bachelor thesis has been carried out by Grischa M. Klimpki

at the

German Cancer Research Center (DKFZ)

under the supervision of

Prof. Dr. rer. nat. Oliver Jäkel

and

Prof. Dr. rer. nat. Uwe Oelfke.

Abstract

Heavy ion radiotherapy offers high dose conformity in the tumor volume while sparing healthy tissue. Because of the inverse dose profile, the maximal dose is deposited in a well-defined, narrow depth range at the distal track end. In order to fully benefit from this sharp dose fall-off, precise knowledge of ion ranges in the patient is substantial. Uncertainties in imaging, in the treatment planning process and in the composition of resulting particle fields due to fragmentation call for reliable in-vivo verification.

Biocompatible fluorescent nuclear track detectors (FNTDs) are promising candidates for high-accuracy in-vivo range measurements and have, therefore, been investigated in this bachelor thesis. Their superior spatial resolution allows for measuring single particle tracks.

Irradiation with protons as well as with carbon, sulfur and magnesium ions at the Max Planck Institute for Nuclear Physics has shown that FNTDs enable the possibility of high-accuracy ion range measurements. Single particle track ranges have been determined with less than 3% deviation from tabulated SRIM values. An automatic track bulk evaluation routine was established for particle fluences greater than 10^7 cm^{-2} yielding the same level of precision.

In a second series of experiments, the basic suitability of FNTDs for clinical in-vivo applications has been analyzed. A treatment plan for a PMMA cylinder containing tissue surrogates and detectors was created and applied at the Heidelberg Ion-Beam Therapy Center. The planned distal edge was compared to the monitored fluorescence profile after proton irradiation. Differences in planned and observed range lay well below the accuracy limiting 1 mm CT slice thickness.

Zusammenfassung

Die Strahlentherapie mit Schwerionen bietet eine sehr gute Abdeckung des Tumervolumens bei gleichzeitiger Schonung gesunden Gewebes. Durch das inverse Dosisprofil der Teilchen wird die maximale Dosis in einem scharf begrenzten Tiefenbereich deponiert. Um von dieser distalen Dosiskante zu profitieren, ist allerdings die genaue Kenntnis von Reichweiten im Patienten unabdingbar. Unsicherheiten in der Bildgebung, im Planungsprozess und in der genauen Zusammensetzung der Teilchenfelder am Zielort aufgrund von Fragmentationsprozessen erzwingen eine verlässliche in-vivo Verifikation.

Da biokompatible, fluoreszierende Kernspurdetektoren (FNTDs) genaue in-vivo Reichweitenmessungen in Aussicht stellen, wurden sie in dieser Bachelorarbeit untersucht. Ihre hohe Ortsauflösung erlaubt den zuverlässigen Nachweis einzelner Kern- und Fragmentspuren.

Die Bestrahlung mit Protonen sowie mit Kohlenstoff-, Magnesium- und Schwefelionen am Max-Planck-Institut für Kernphysik hat gezeigt, dass sich FNTDs exzellent für Reichweitenmessungen eignen. Reichweiten einzelner Kernspuren wurden mit weniger als 3% Abweichung von tabellierten Werten (SRIM) ermittelt. Außerdem konnte eine Auswertungsroutine für Detektoren, die mit Fluenzen $\Phi > 10^7 \text{ cm}^{-2}$ bestrahlt wurden, ohne Genauigkeitsverlust automatisiert werden.

In einer zweiten Reihe von Experimenten wurde darauf aufbauend analysiert, ob sich FNTDs grundsätzlich auch für in-vivo Reichweitenmessungen eignen. Am Heidelberger Ionenstrahl-Therapiezentrum wurde für einen PMMA-Zylinder, der neben Gewebeersatzmaterialien auch Kernspurdetektoren enthielt, ein Bestrahlungsplan erstellt und appliziert. Die geplante distale Kante wurde nach der Protonenbestrahlung mit dem aufgezeichneten Fluoreszenzprofil im Detektor verglichen. Die Unterschiede zwischen geplanter und beobachteter Reichweite lagen weit unter der genauigkeitslimitierenden CT-Schichtdicke von 1 mm.

CONTENTS

1	Introduction	1
2	Fundamental Quantities	3
2.1	Ionizing radiation	3
2.2	Particle fluence	3
2.3	Absorbed dose	4
2.4	Linear stopping power	4
2.5	Linear energy transfer	5
2.6	Projected range	5
3	Materials and Methods.....	9
3.1	Fluorescent nuclear track detectors.....	9
3.1.1	Introduction	9
3.1.2	Crystal structure and defect properties	10
3.1.3	Confocal microscopy based readout	12
3.1.4	Further advantages of FNTDs.....	13
3.2	Irradiation facilities	13
3.2.1	Max Planck Institute for Nuclear Physics (MPI-K).....	13
3.2.2	Heidelberg Ion-Beam Therapy Center (HIT)	14
3.3	Zeiss LSM 710	14
3.3.1	Light path, filters and detectors	14
3.3.2	Control parameters	15
3.4	Siemens SOMATOM Sensation 4 CT Scanner	16
3.5	Tissue surrogates	16
3.6	Data processing and evaluation	17
4	Experiments	19
4.1	High-accuracy ion range measurements	19
4.1.1	Experimental setup	19
4.1.2	Particles and fluences.....	19
4.1.3	Image acquisition.....	21
4.2	In-vivo range measurements.....	22
4.2.1	Estimation of lateral scattering.....	22
4.2.2	CT scans of the PMMA phantom	23
4.2.3	Contouring and planning	24
4.2.4	Irradiation at HIT	27
4.2.5	Detector readout	28

5	Results	29
5.1	High-accuracy ion range measurements	29
5.1.1	Single track evaluation	29
5.1.2	Automated bulk evaluation	31
5.1.3	Influence of pinhole diameter.....	33
5.1.4	Summarized range results	34
5.1.5	Dose intensity correlation.....	35
5.2	In-vivo range measurements.....	37
5.2.1	Distal edge comparison	37
5.2.2	Summarized range results	39
6	Discussion and Outlook	41
6.1	Range measurements based on single track evaluation	41
6.1.1	Results of the single track evaluation.....	41
6.1.2	Influence of the nuclear stopping power component.....	41
6.2	Range measurements based in automated bulk evaluation	42
6.2.1	Results of the track bulk evaluation.....	42
6.2.2	Quenching effect.....	42
6.3	In-vivo range measurements.....	43
6.3.1	Results of the in-vivo range measurements	43
6.3.2	WEPL measurements	44
6.4	Suggestions for further experiments.....	44
6.4.1	In-vivo irradiation under pre-clinical conditions.....	44
6.4.2	In-vivo irradiation with carbon ions.....	45
6.4.3	Dose calibration curves for protons and carbon ions.....	45

Appendix

A	Lists.....	i
A.1	List of abbreviations.....	i
A.2	List of symbols.....	i
A.3	List of figures.....	ii
A.4	List of tables.....	iv
A.5	List of experiments	iv
B	Readout protocols and images	v
B.1	FNTDs irradiated at MPI-K.....	v
B.2	CT images of the PMMA phantom.....	xii
B.3	FNTDs irradiated at HIT	xiv
C	Workflow excerpts	xxi
C.1	FNTD range measurements in ImageJ	xxi
C.2	Treatment planning at HIT.....	xxiii
C.2.1	Contouring on Siemens patient system	xxiii
C.2.2	Treatment planning under Tx.....	xxv
D	Bibliography.....	xxxix

1 INTRODUCTION

Radiation therapy with heavy charged particles (HCPs) such as protons and carbon ions has gained increasing interest over the past years. Its main assets are the inverse dose profile with a defined range yielding superior dose conformity and the high ionization density giving a differential biological effect between tumor and healthy tissue. However, incomplete tissue knowledge as well as uncertainties in patient imaging, in the treatment planning process and in resulting particle fields due to fragmentation can largely jeopardize the potential clinical benefit.

Treatment plans for ion radiotherapy undergo quality assurance on numerous levels before being applied. Particle fluence and energy are optimized on planning computers to achieve the desired dose distribution in malignant tissue taking scattering cross-sections into account. The machine delivery itself is constantly being supervised. Currently, the final step is the verification of the forward calculated individual treatment plan in a water phantom, but there are still only limited means for in-vivo verifications (e.g. PET and prompt gamma).

Novel fluorescent nuclear track detectors (FNTDs) based on biocompatible aluminum oxide crystals are promising candidates for in-vivo range and fragmentation monitoring. Their superior spatial resolution allows for measuring single particle tracks. At the same time, FNTDs might serve as x-ray markers because of their high density. In this thesis, the basic suitability of FNTDs for clinical in-vivo applications has, therefore, been investigated.

In a first series of experiments, FNTDs have been irradiated with carbon, magnesium and sulfur ions at the Max Planck Institute for Nuclear Physics (section 4.1) to compare previous successful single range measurements with new bulk evaluation techniques (section 5.1). The second experiment serves as a precursor of later in-vivo FNTD applications. The entire treatment planning process was applied to a PMMA cylinder with six different insert combinations – from CT scans over contouring and planning to the actual proton irradiation at the Heidelberg Ion-Beam Therapy Center (section 4.2). The predicted distal edge in the implanted detector can be verified via bulk range measurements (section 5.2).

Fundamental quantities with relevance to the measurements conducted are introduced in chapter 2. Physical properties of $\text{Al}_2\text{O}_3:\text{C}, \text{Mg}$ crystals and used tissue surrogates as well as irradiation facilities and readout tools are described in chapter 3. Experimental setups and the obtained results are given in chapter 4 and 5. Chapter 6 contains a final summary and discussion.

2 FUNDAMENTAL QUANTITIES

The International Commission on Radiation Units and Measurements (ICRU) defined fundamental quantities for ionizing radiation in their 60th report (1998 [11]). Those of importance for this thesis will be outlined in this chapter.

2.1 Ionizing radiation

The process of radiation refers to particles or waves transporting energy through a medium or space. If one or more electrons are liberated in collisions with atoms or molecules, one speaks of ionizing radiation. The likelihood of ionization decreases with decreasing particle velocity (energy). The principle aim of using ionizing radiation in therapy is to stop unregulated cell growth where chemotherapy or surgery cannot be applied.

2.2 Particle fluence

The particle fluence Φ at a point \vec{r} in space is defined as the number dN of particles incident on a sphere of cross-sectional area dA_{\perp} :

$$\Phi(\vec{r}) := \frac{dN}{dA_{\perp}} \left[\frac{1}{\text{cm}^2} \right] \quad (2.1)$$

A sphere has been used in this definition to express that one considers an area dA_{\perp} perpendicular to the direction of each particle. If beam particles are unidirectional, on parallel, unaltered trajectories and homogeneously distributed within the beam, the expression for the fluence simplifies to the total number N of particles penetrating a finite perpendicular area A_{\perp} :

$$\Phi = \frac{N}{A_{\perp}} \quad (2.2)$$

Equation 2.2 applies to most experimental setups of this thesis. The particle fluence Φ can simply be determined by measuring the total number of particles N .

2.3 Absorbed dose

Energy conservation for a single interaction i in matter yields:

$$\epsilon_i = \epsilon_{in} - \epsilon_{out} + Q, \quad (2.3)$$

where ϵ_i is the deposited energy, ϵ_{in} is the kinetic energy of the incident ionizing particle, ϵ_{out} is the sum of the kinetic energies of all ionizing particles leaving the interaction and Q is the change in the rest energies of the nucleus and of all particles involved in the interaction.

The total imparted energy ϵ to matter in a given volume of a single ionizing particle is the sum of all deposited energies ϵ_i due to multiple interactions:

$$\epsilon = \sum_i \epsilon_i \quad (2.4)$$

At clinical fluences millions of ionizing particles enter the target volume. The absorbed dose D measures the mean energy imparted $d\bar{\epsilon}$ to matter of mass dm , thus

$$D := \frac{d\bar{\epsilon}}{dm} [\text{Gy}]. \quad (2.5)$$

One gray is defined as the absorption of one joule of ionizing radiation by one kilogram of matter:

$$1 \text{ Gy} := 1 \frac{\text{J}}{\text{kg}} \quad (2.6)$$

FNTDs monitor electronic interactions since secondary electrons are being captured in color centers. The observed fluorescence signal, therefore, correlates to the sum of all deposited energies ϵ .

2.4 Linear stopping power

When traversing a medium, particles will lose their kinetic energy and finally come to rest. The linear stopping power quantifies this process for charged particles in neutral materials. It is defined as the quotient of lost kinetic energy dE by the traversed distance dl :

$$S := \frac{dE}{dl} \left[\frac{\text{MeV}}{\text{cm}} \right] \quad (2.7)$$

Three major components contribute to the total linear stopping power S depending on the interaction of incident particles with the matter penetrated:

- The linear electronic stopping power S_{el} considers inelastic collision with electrons.
- The linear radiative stopping power S_{rad} is due to emission of bremsstrahlung in the electric field of atomic nuclei or atomic electrons and, therefore, only of relevant magnitude if electrons are the incident particles.
- The linear nuclear stopping power S_{nuc} takes elastic Coulomb collisions with heavy nuclei into account. Recoil energy is imparted to target atoms. In addition, one can also consider energy losses due to inelastic nuclear processes.

The linear stopping power can be written as a sum of all three terms:

$$S = S_{el} + S_{rad} + S_{nuc} \quad (2.8)$$

The electronic component is of major significance for ion range measurements in this thesis because radiochromatic transformation in FNTDs is triggered by electronic rather than nuclear processes.

2.5 Linear energy transfer

In hadron therapy, one is interested in the ionization density along the particle trajectory. Secondary electrons or δ -electrons carry away kinetic energy from the regarded cell volume. The linear energy transfer (LET) has been introduced in search of a quantity that connects physical energy transfer with biological cell response more directly than dose. It is defined as the difference of the linear electronic stopping power S_{el} and the sum of the kinetic energies of all released electrons:

$$\text{LET}_\Delta := S_{el} - \frac{dE_\Delta^\delta}{dl} \left[\frac{\text{keV}}{\mu\text{m}} \right] \quad (2.9)$$

The sum of the kinetic energies dE_Δ^δ has to be greater than a specific energy cutoff Δ . Secondary electrons with kinetic energies smaller than Δ are still considered to be part of the HCP track core. The energy cutoff can, therefore, be regarded as a pipe around the particle track. Only energy transferred to secondary electrons leaving the pipe is subtracted from the linear electronic stopping power S_{el} .

2.6 Projected range

HCPs traversing matter continuously slow down due to momentum transfers. In order to calculate the projected range R of an incident particle in a target material

one has to integrate the inverse linear stopping power S^{-1} over all kinetic energies E in the interval $[E_{max}, E_{min}]$:

$$R := \int_{E_{max}}^{E_{min}} \frac{dE}{S} \text{ [cm]} \quad (2.10)$$

The upper limit of the integral cannot be zero since $S(0) = 0$. Incident particles at rest will not impart energy. Therefore, a minimal cut-off energy E_{min} is introduced. Because very low particle energies only have minor contributions to the total projected range, equation 2.10 is a reasonable range definition.

In this thesis, the calculation of inverse dose profiles is based on tabulated SRIM data (Stopping and Range of Ions in Matter, J.F. Ziegler, 2012 [22]) and the continuous slowing down approximation (CSDA) assuming that incident particles gradually impart their energy in small range intervals of width ΔR_n . As figure 2.1 shows, incident particles enter the regarded voxel with a kinetic energy E_n and leave it with $E_{n+1} < E_n$. The linear stopping power is presumed constant and can be calculated as a mean of S_n and S_{n+1} , where S_n and S_{n+1} are the corresponding linear stopping powers to E_n and E_{n+1} . They can be obtained from SRIM tables.

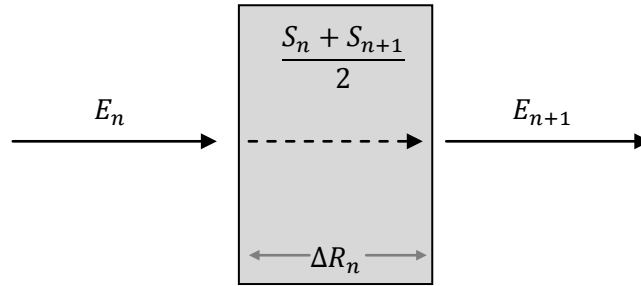


Figure 2.1 CSDA for particles traversing small volumes of width ΔR_n

For the calculation of the depth-dose curves, 1% energy loss per range interval was chosen meaning:

$$E_n = 0.99^n E_0 \text{ and} \quad (2.11)$$

$$\Delta R_n = 2 \frac{E_n - E_{n+1}}{S_n + S_{n+1}} \quad (2.12)$$

E_0 is the initial kinetic energy of the particle beam. If one additionally assumes constant particle fluence Φ throughout the detector, the absorbed dose can be calculated in each volume via

$$D_n = \frac{S_n + S_{n+1}}{2\rho} \Phi \quad (2.13)$$

ρ is the physical density of the target material. This iteration was applied until a cutoff energy of 1 keV was reached. Figure 2.3 shows the resulting depth-dose curve of 100 MeV/u carbon ions in polymethyl methacrylate (PMMA).

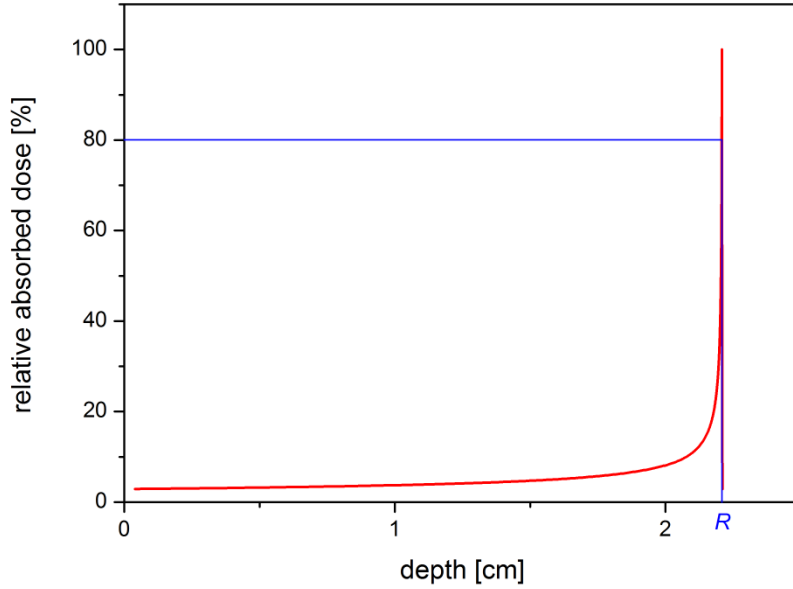


Figure 2.2 SRIM calculated depth-dose curve of a 100 MeV/u carbon ion beam in PMMA

The relative absorbed dose D/D_{max} is plotted against the traversed distance in the target. The projected range R can also be defined as the depth in which the relative absorbed dose reaches the 80% threshold. This is visualized by the blue line. Monte Carlo calculations also consider straggling resulting in a broader Bragg peak. A FLUKA (A. Fassò, 2012 [6]) simulated depth-dose curve can be seen in figure 2.3.

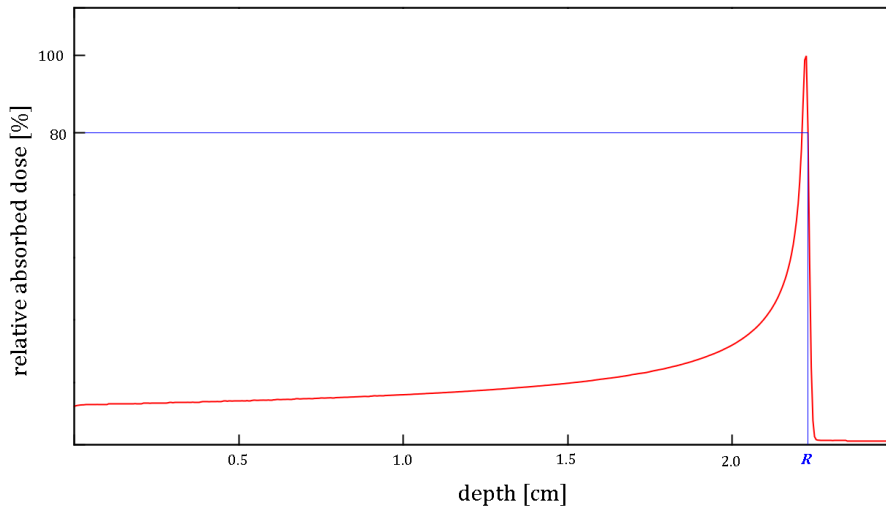


Figure 2.3 FLUKA simulated depth-dose curve of a 100 MeV/u carbon ion beam in PMMA

3 MATERIALS AND METHODS

Fluorescent nuclear track detector (FNTD) technology is presented in this chapter. Detector properties and characteristics are discussed in section 3.1. Experiments involved irradiation at two different facilities (section 3.2). Irradiated detectors were read out with the confocal laser-scanning microscope described in section 3.3. CT scans of FNTDs and tissue surrogates (section 3.5) were done on the Siemens SOMATOM Sensation 4 (section 3.4). The evaluation of microscope and CT images used data processing techniques outlined in section 3.6.

3.1 Fluorescent nuclear track detectors

3.1.1 Introduction

Novel fluorescent nuclear track detectors (FNTDs), recently developed and demonstrated by Landauer Inc., have originally been designed for high capacity volumetric optical data storage. Based on single aluminum oxide crystals doped with carbon and magnesium, FNTDs contain very high concentrations of aggregate oxygen vacancy defects which stimulate the production of new color centers during crystal growth. Because these color centers exhibit radiochromatic transformations under ionizing radiation, FNTDs show excellent detection efficiency of fast neutrons and swift heavy charged particles. For this study, samples from single $\text{Al}_2\text{O}_3:\text{C, Mg}$ crystals were cut along the optical c -axis into small rectangular plates ($4.0 \times 6.0 \times 0.5 \text{ mm}^3$) and polished on one of their large sides to obtain an optically transparent surface.

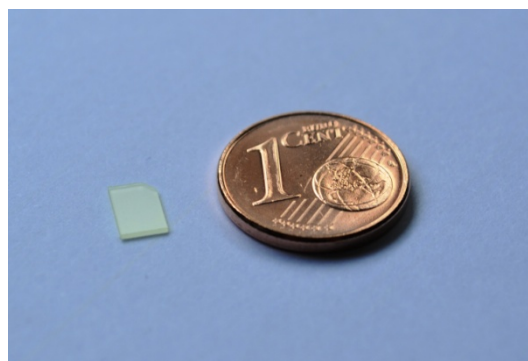


Figure 3.1 Size of a FNTD compared to a one cent coin

3.1.2 Crystal structure and defect properties

In $\alpha\text{-Al}_2\text{O}_3$ crystals (corundum) the O^{2-} ions form a rigid, slightly distorted hexagonal-close-packed sublattice. Two out of every three octahedral interstices are occupied by an Al^{3+} ion. This means that each O^{2-} ion is surrounded by four tetrahedral nearest-neighbor Al^{3+} ions and each Al^{3+} ion is surrounded by six O^{2-} ions as shown in figure 3.2. $\alpha\text{-Al}_2\text{O}_3$ has a physical density of 3.98 g/cm^3 .

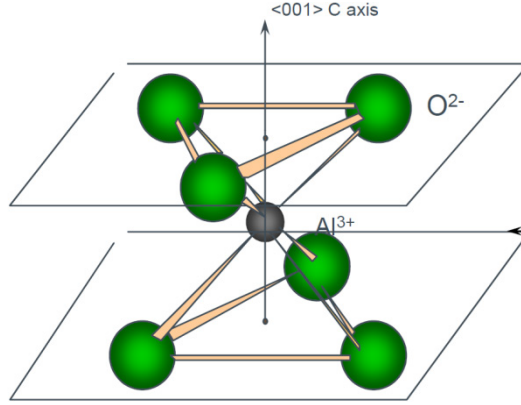


Figure 3.2 Crystal structure of corundum ($\alpha\text{-Al}_2\text{O}_3$); reprinted from [3]

Desired $\text{Al}_2\text{O}_3\text{:C,Mg}$ single crystals are grown from the melt in a highly reduced atmosphere at low partial pressure of oxygen using the Czochralski method (M.S. Akselrod, 2003 [2]): Aluminum oxide powder is melted in a crucible and dopant impurity atoms (C and Mg) are added. A precisely along the optical c -axis oriented rod-mounted $\text{Al}_2\text{O}_3\text{:C,Mg}$ seed crystal is then dipped into the molten material, slowly pulled upwards and rotated simultaneously. The crystallization process at the seed surface is controlled by strong temperature gradients, the pulling rate and the speed of rotation. As a result, a large $\text{Al}_2\text{O}_3\text{:C,Mg}$ single crystal can be extracted.

Being grown in a reduced atmosphere, this crystal will contain numerous aggregate oxygen vacancy defects throughout its lattice. The absence of an O^{2-} ion leads to a strong local charge imbalance. Because two electrons can be trapped in such a vacancy, it is denoted as a F^{2+} color center. The majority of these color centers contains one electron:



In order to charge-compensate the remaining imbalance Al^{3+} ions are substituted by Mg^{2+} ions yielding a net local charge of -1 . It is believed that two one-electron F^+ color centers are always surrounded by two Mg^{2+} ions forming a two-electron $\text{F}_2^{2+}(2\text{Mg})$ color center as depicted in figure 3.3 (G.M. Akselrod, 2006 [1]).

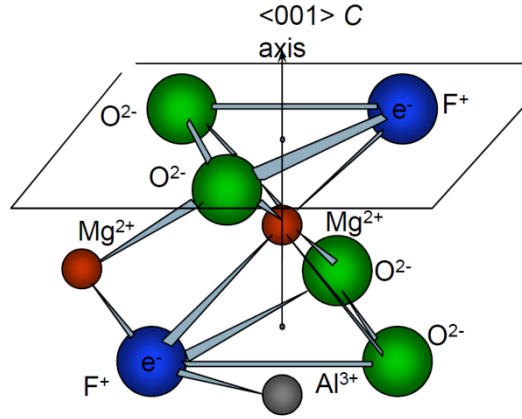
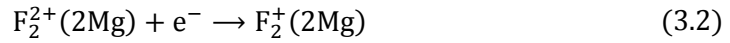


Figure 3.3 Model of the $F_2^+(2Mg)$ aggregate defect; reprinted from [3]

The passage of a charged particle through the crystal lattice leads to ionization. Holes are created in the valance band and free electrons in the conduction band which are then trapped in color centers producing radiochromatic transformation:



Transformed $F_2^+(2Mg)$ color centers have three excited states identified by their absorption bands centered at 4.8 eV (260 nm), 3.7 eV (335 nm) and 2.0 eV (620 nm). They produce fluorescence at 750 nm under optical excitation with a high quantum yield and a short lifetime of $\tau = 75 \pm 5$ ns. Untransformed $F_2^{2+}(2Mg)$ color centers, on the other hand, absorb in the blue region (435 nm) and emit 520 nm photons giving the as-grown crystals their green-yellow coloration (G.J. Sykora, 2010 [20]). This significant difference is emphasized in figure 3.4.

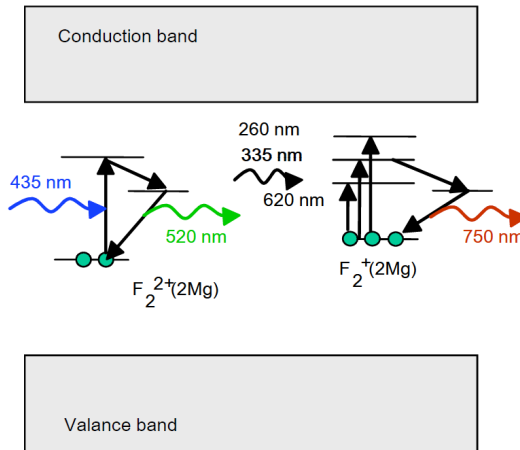


Figure 3.4 Absorption and fluorescence of $F_2^{2+}(2Mg)$ and $F_2^+(2Mg)$ color centers; reprinted from [2]

The broad variety of excitation and emission bands of $\text{Al}_2\text{O}_3:\text{C}, \text{Mg}$ crystals has been investigated by Sykora and Akselrod (2010 [20]). Their results are listed in table 3.1.

excitation wavelength	emission wavelength	crystal defect
240 nm	325 nm	$\text{F}^+(\text{Mg})$
255 nm	325 nm	$\text{F}^+(\text{Mg})$
260 nm	750 nm	$\text{F}_2^+(2\text{Mg})$
300 nm	500 nm	F_2
335 nm	750 nm	$\text{F}_2^+(2\text{Mg})$
350 nm	385 nm	$\text{F}_2^+(\text{Mg})$
435 nm	510 nm	$\text{F}_2^{2+}(2\text{Mg})$
620 nm	750 nm	$\text{F}_2^+(2\text{Mg})$

Table 3.1 Excitation and emission bands of $\text{Al}_2\text{O}_3:\text{C}, \text{Mg}$ crystals

3.1.3 Confocal microscopy based readout

Color centers undergo radiochromatic transformation along incident particle tracks because of secondary electron capture. When stimulated with a red laser (620 nm), these radiation-induced tracks appear as bright fluorescent features on dark background. Therefore, the FNTD readout is based on laser-induced fluorescence (also known as photo-luminescence) and not optically stimulated luminescence. Because of superior spatial resolution, individual ion tracks can be imaged using a laser scanning confocal fluorescence microscope allowing non-destructive readout.

The microscope laser causes the transformed color centers of one distinct layer to fluoresce. This signal is then detected with avalanche photo-diodes and amplified. The confocal pinhole acts as a spatial filter, blocking all fluorescence originating outside of the focal spot of the objective lens. Obtaining data from numerous layers allows reconstructing 3D images of single tracks through the detector volume. Because the actual diameter of the track penumbra is in the order of several μm depending on the particle atomic number and its energy, randomly distributed tracks can be imaged without significant overlap at track densities of at least 10^6 cm^{-2} (G.M. Akselrod, 2006 [1]).

Short fluorescence lifetime allows for fast laser scanning and high-productivity imaging. FNTDs are also sensitive to charged particles with very low LET (approximately $0.1 \text{ keV}/\mu\text{m}$) including secondary electrons. The track detection efficiency for protons and heavy ions lies at nearly 100% (G.M. Akselrod, 2006 [1]). After non-destructive and completely optical readout with no chemical etching or other detector preparation, fluorescent tracks can be erased from the FNTD by thermally annealing the detector material at approximately 680°C for 10 – 15 minutes (M.S. Akselrod, 2006 [4]).

3.1.4 Further advantages of FNTDs

FNTDs are passive integrating detectors which do not require wires, electronics or batteries during irradiation. They are cut from single aluminum oxide crystals. Al_2O_3 is a wide gap insulator with $E_g = 9.5 \text{ eV}$ and, therefore, a highly stable and inert material also in harsh environments such as vacuum (G.M. Akselrod, 2006 [1]). Discussed electron trapping centers are deep, thermally stable up to 600°C and immune to unwanted electromagnetic interferences. The spatial imaging resolution and the ability to non-destructively obtain 3D depth-dose distributions are major superiorities over conventionally processed CR-39 plastic nuclear track detectors.

Aluminum oxides biocompatibility opens new possibilities for quality assurance in radiotherapy and diagnostic imaging. Implanted detectors or detectors in body cavities can help accessing direct information on a radiation treatment such as ion fluences, energies or ranges using fully automated and sophisticated processing routines. Irradiations of FNTDs at the Heidelberg Ion Beam Therapy Center within this study serve as a precursor of later in-vivo FNTD applications.

3.2 Irradiation facilities

3.2.1 Max Planck Institute for Nuclear Physics (MPI-K)

The MPI-K, one out of 80 institutes of the Max Planck Society, offers a large number of ion sources. The accelerator complex consists of a flexible system of five different particle accelerators. Therefore, almost every type of ion beam can be provided over a large fluence range, also at low energies (MPI-K, 2012 [13]).

In the first series of experiments, FNTDs were irradiated with C-12, Mg-24 and S-32 ions. The 12 MV Tandem van-de-Graaff Accelerator established total kinetic energies of 48, 98 and 100 MeV, respectively.

3.2.2 Heidelberg Ion-Beam Therapy Center (HIT)

The HIT is the first hospital-based treatment facility at a clinic in Europe where patients can be treated with protons as well as with carbon ions. The particle beam is accelerated in a synchrotron and guided into one of the three treatment rooms by strong magnets. At HIT, a new radiation method known as the “intensity-controlled rasterscan technique” offers the highest level precision in the three-dimensional radiation of tumors. Pencil beams follow the tumor contour while cross sections of the tumor are divided into several beam positions. Beam spots have an approximately Gaussian-shaped lateral profile. Available energy ranges from 48 to 221 MeV for protons and 89 to 430 MeV/u for carbon ions correspond to a water range of 2 to 31 cm (Heidelberg University Hospital, 2012 [9]).

3.3 Zeiss LSM 710

In this study, the Zeiss LSM710 inverted design laser scanning microscope provided by the light microscopy facility at DKFZ was used together with the 2009 ZEN control software for FNTD readout. The principles of confocal microscopy and the characteristics of the LSM 710 (Zeiss, 2009 [5]) will be discussed in the following.

3.3.1 Light path, filters and detectors

Confocal microscopy enables optical sectioning of the specimen by using a detector pinhole. Excitation of color centers is stimulated with a 633 nm Helium-Neon laser line (5 mW) resulting in emission of 750 nm fluorescence. As shown in figure 3.5, the laser light passes a multi-band beam splitter (MBS488/561/633) before being focused on the specimen by an objective lens (40x / 1.4 Oil DIC II). Because of the finite pinhole diameter, true point illumination cannot be achieved. The light cone also stimulates fluorescence behind and in front of the focal plane yielding an effective slice thickness δ_z . Fluorescence light passes the objective lens and the beam splitter (dichroic mirror). A tube lens focuses the emitted light on the pinhole, a circular aperture obstructing light rays off focus. The pinhole diameter d , therefore, limits the axial detection volume. Three photomultipliers (PMTs) and two fiber-coupled avalanche photodiodes (APDs) count fluorescence intensity. APDs are necessary because PMTs have very low quantum efficiency in the red. Scanning mirrors attached to piezoelectric crystals enable lateral deflection of laser and fluorescence light. A motor driven microscope stage realizes full 3D imaging.

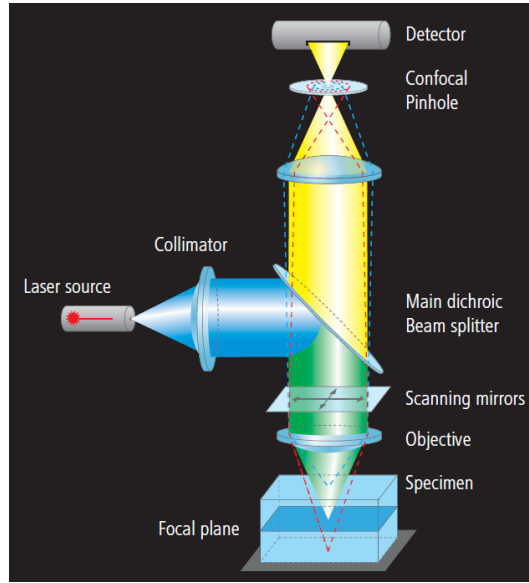


Figure 3.5 Schematic diagram of the Zeiss LSM 710 light path; reprinted from [5]

3.3.2 Control parameters

The ZEN software allows controlling the following parameter for read out:

- The digital gain g and the digital offset Δg change the gray scale on histogram representation within ZEN. Since they do not influence the actual APD counting, they were kept at optimal settings of $g = 0.20$ and $\Delta g = 0.00$.
- The vertical and horizontal field size l_x and l_y determine the lateral dimensions of the image at variable pixel resolutions.
- The dwell time τ ranging from 1.27 to 177.32 μs defines how long the laser illuminates one spot position. It, therefore, influence the total number of detected photons N .
- N can also be accumulated over a certain number of rescans $R = 1 \dots 16$.
- The relative excitation laser power p can be reduced in order to prevent APDs from shutting down. For protection reasons, the photon counting rate is limited to $\eta_{max} = 4 \text{ MHz}$.
- The pinhole diameter d defines the slice thickness δ_z of an image.
- When acquiring numerous images in depth, the step size Δz is another important parameter.

Dwell time τ , number of rescans R and relative laser power p have to be chosen according to scan time and desired noise signal ratios. During readout, FNTDs were always stored in glass bottom microwell dishes from MatTek Corp., Ashland, MA,

USA (Part No. P35G-1.5-20-C) to keep them free from immersion oil. All images were taken in 16 bit color depth preserving the maximal dynamic range of $N_{max} = 65535$ (S. Greulich, *in prep.* [8]).

3.4 Siemens SOMATOM Sensation 4 CT Scanner

CT scans of the PMMA cylinder were done at the Kopfklinik, Heidelberg University Hospital, on a Siemens SOMATOM Sensation 4 CT Scanner (Siemens, 2011 [18]). It offers rotation times as fast as 500 ms and can do 160 slices in 20 seconds breathhold with a reconstruction time of 1.5 slices per second. The *syngo* application platform is also used at HIT. All CT scans used the ion RT protocol “01_HIT_BPL_Schaedel_S4” to ensure standard imaging. The tube current was fixed to 264 mAs (H40s kernel) at a voltage of 120 kVp. A slice thickness of 1 mm was chosen in order to achieve the highest distal resolution offered.

3.5 Tissue surrogates

In the second series of experiments, FNTDs were placed in a polymethyl methacrylate (PMMA) cylinder (length $L = 44.8$ cm, outer radius $R = 8.0$ cm and inner radius $r = 14.2$ mm) behind different insert rods. PMMA has a physical density of 1.18 g/cm³. A sketch of the cylinder can be seen in figure 3.6.

The insert rods were made of PMMA and tissue-equivalent materials. The tissue surrogates shown in figure 3.7 are part of the Tissue Characterization Phantom 467 manufactured by Gammex Inc. (2012 [7]). They mimic the elemental compositions of real tissues and their cross sections for diagnostic photon radiation. The manufacturer provides a specification sheet with physical and electron densities (compared to water):

Gammex insert	relative electron density ρ_e/ρ_e^w	physical density ρ [g/cm ³]
Lung (LN-450)	0.40	0.45
Adipose (AP6)	0.90	0.92
Liver (LV1)	1.07	1.08
Bone (CB2-30%)	1.28	1.34

Table 3.2 Physical and electron densities of Gammex inserts; reprinted from [7]

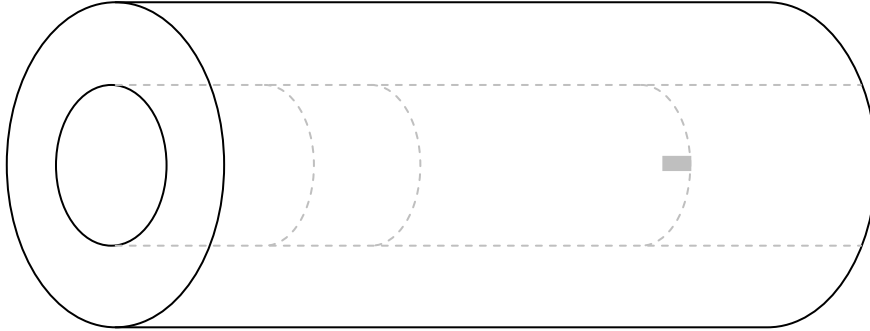


Figure 3.6 Schematic diagram of the PMMA cylinder



Figure 3.7 Gammex inserts: adipose, lung, cortical bone and liver

3.6 Data processing and evaluation

Microscope images were processed using ImageJ (version 1.46a), a public domain Java program developed by Wayne Rasband (2012 [17]). The plug-in "Stack profile Plot" by Pariksheet Nanda saves the intensity profile of all images in a stack to a .txt file (P. Nanda, 2012 [17]). For further analysis, these text files were imported to R, a free software program for statistical computation. The R versions used in this thesis were 2.14 and higher (R Core Team, 2012 [14]). Visualization of final data and the creation of plots were done with OriginPro 8.6G.

Obtained DICOM (Digital Imaging and Communications in Medicine) data were visualized with the open-source software MITK-3M3 (version 1.1) developed by the division of Medical and Biological Informatics at DKFZ and mint medical (2012 [14]).

All Monte Carlo simulations have been carried out on FLUKA (copyright INFN and CERN). FLUKA is a fully integrated particle physics Monte Carlo simulation package. Original authors are Alberto Fassò, Alfredo Ferrari, Johannes Rantf and Paolo Sala et al (2012 [6]). Discrete stopping power or range values were taken from J.F. Ziegler's SRIM (Stopping and Range of Ions in Matter) software – version 2012.01 [22].

4 EXPERIMENTS

In order to measure projected ranges at low and clinical fluences, FNTDs have been irradiated at the Max Planck Institute for Nuclear Physics (MPI-K) with carbon, magnesium and sulfur ions. The experimental setup and the irradiation parameters are outlined in section 4.1. Section 4.2 describes the standard treatment procedure – from CT scans over contouring and planning to the actual proton irradiation at the Heidelberg Ion-Beam Therapy Center (HIT).

4.1 High-accuracy ion range measurements

4.1.1 *Experimental setup*

FNTDs were placed on an aluminum holder as seen in figure 4.1. The holder was then suspended in a vacuum chamber facing the particle beam. FNTDs were, therefore, irradiated parallel to their large sides.



Figure 4.1 FNTD being placed on position 8

4.1.2 *Particles and fluences*

The particle fluence was controlled over a Faraday cup that could be moved in and out of the ion beam (comp. figure 4.2). In order to keep the cup on a constant potential, electrons have to neutralize the charge z of attracted cations. This cup current increases linearly with increasing particle fluence. The MPI-K states that a cup current of $z \cdot 100$ pA equals 0.6×10^9 ions per second. By changing the beam

widening through quadrupole magnets and the total irradiation time, the desired fluences could be achieved. Note that the ion beam has an area of 1 cm^2 because of quadratic apertures and was assumed to be homogenous at all times. The irradiation protocol is listed in table 4.1.

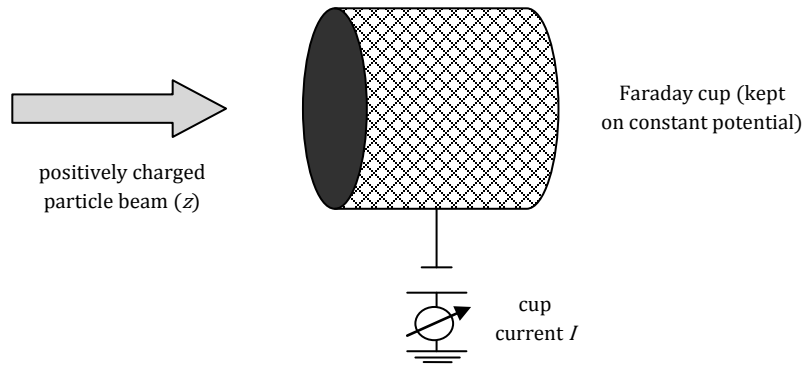


Figure 4.2 Schematic diagram of the Faraday cup

FNTD number	particle (charge)	total kinetic energy [MeV]	cup current [pA]	irradiation time [s]	expected particle fluence [cm^{-2}]
gk1000	C-12 (5+)	48.0	0.643	1.00	7.7×10^5
gk1001	C-12 (5+)	48.0	166.7	500	1.0×10^{11}
gk1002	S-32 (9+)	100	0.500	2.00	6.7×10^5
gk1003	C-12 (5+)	48.0	0.643	4.00	3.1×10^6
gk1004	C-12 (5+)	48.0	0.643	40.0	3.1×10^7
gk1005	C-12 (5+)	48.0	16.67	5.00	1.0×10^8
gk1006	C-12 (5+)	48.0	16.67	50.0	1.0×10^9
gk1007	C-12 (5+)	48.0	16.67	500	1.0×10^{10}
gk1008	S-32 (9+)	100	300.0	500	1.0×10^{11}
gk1009	Mg-24 (8+)	96.0	0.200	3.00	4.5×10^5
gk1010	Mg-24 (8+)	96.0	266.7	500	1.0×10^{11}

Table 4.1 MPI-K irradiation protocol

4.1.3 Image acquisition

Irradiated detectors were read out with the Zeiss LSM 710 confocal microscope introduced in section 3.3. The dwell time τ , the pixel matrix and the relative laser power p were adjusted for each detector to achieve optimal imaging parameters. Detectors irradiated with low and high fluences have generally been distinguished in readout procedure. A detailed readout protocol and an overview of acquired images can be found in appendix B.1.

- For fluences smaller than 10^7 cm^{-2} , single particle tracks were well visible under the microscope. 34 images were taken in depth to ensure that track core centers lie in the focal plane. This will allow for precise range measurements (comp. section 5.1.1). An exemplary image of single tracks can be seen in figure 4.3.

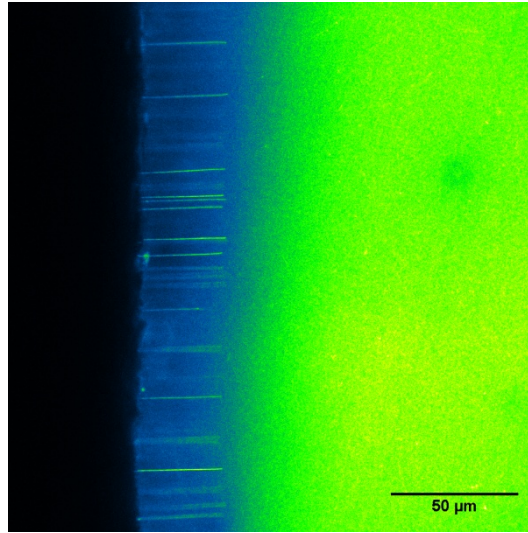


Figure 4.3 3.1×10^6 carbon ions per cm^2 with track cores on and off focus
(1024×1024 pixels, $100.85 \mu\text{s}$ dwell time and 100% relative laser intensity)

- For fluences greater than 10^7 cm^{-2} , single tracks could no longer be resolved. Therefore, a larger area of the detector edge was imaged in only one depth. This was done by combining several single images in a so called tile scan. The automated evaluation routine of these pictures is explained in section 5.1.2.

In a second readout, the pinhole diameter was reduced to cut off fluorescent light originating outside of the focal plane. The influence of the pinhole diameter on the accuracy of range measurements is examined in section 5.1.3.

4.2 In-vivo range measurements

4.2.1 Estimation of lateral scattering

FNTDs were placed in a PMMA phantom to compare the planned dose distribution with the actual fluorescence profile in the detector. The treatment planning software allows creating a clinical target in front of the detector which will be irradiated homogeneously. Because aluminum oxide is a highly dense material compared to PMMA, particles will have a much shorter range in the detector. In order to estimate the range difference and the lateral scattering in and out of the detector material, a FLUKA simulation based on so called Monte Carlo calculations was set up. This simulation will help defining the position of the clinical target in front of the FNTDs so that the distal edge is well visible in the detector after irradiation.

The circular area of a PMMA cylinder (length $L = 44.8$ cm and radius $R = 8.0$ cm) was irradiated with a rectangular 142 MeV/u proton beam ($\Delta x = \Delta y = 2$ cm). Three FNTDs were placed at 12 cm depth so that their small side (4.0×0.5 mm²) was facing the proton beam. This is depicted in figure 4.4.

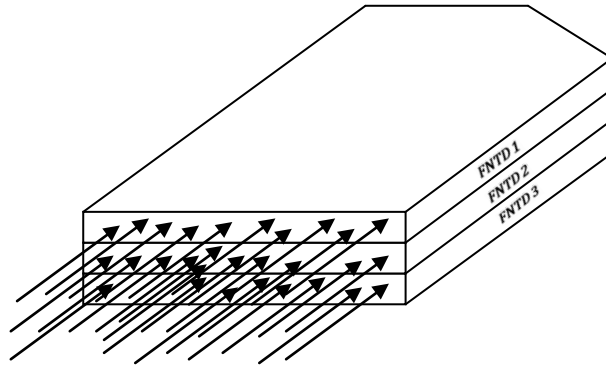


Figure 4.4 Schematic diagram of the FNTD irradiation at HIT

FNTD material was assigned as aluminum oxide and the phantom cylinder as pre-defined PMMA. The energy threshold for secondary particles was set to 100 keV/u while the heavy ion transport protocol was used on a precision simulation. The two dimensional depth-dose distribution for 10^9 primaries shows significant lateral scattering influence in the surrounding FNTDs (labeled with 1 and 3 in figure 4.5). The centered detector appears to have a homogeneous dose distribution. Two phantom FNTDs were, therefore, assumed to be sufficient to reduce scattering effects in the detector which will be read out under the confocal microscope (labeled with 2 in figure 4.5).

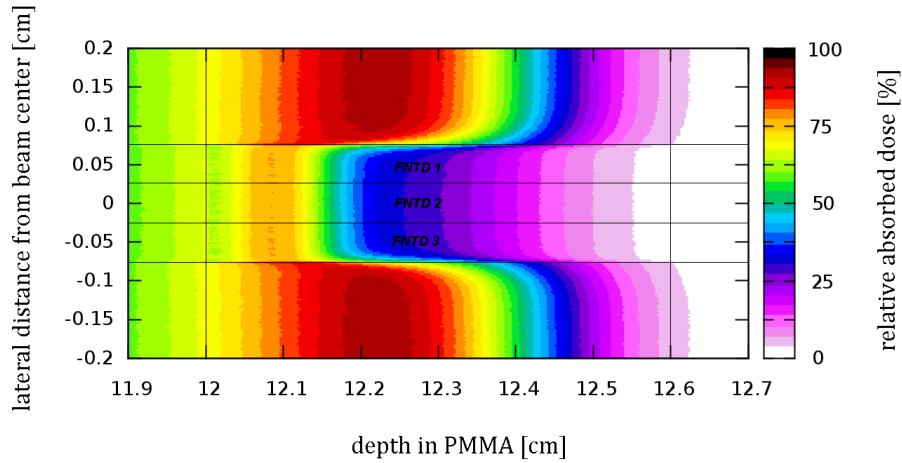


Figure 4.5 FLUKA simulated two dimensional depth-dose distribution

4.2.2 CT scans of the PMMA phantom

CT scans of six different insert combination listed in table 4.2 have been obtained with the Siemens SOMATOM Sensation 4 CT Scanner (Kopfclinik, Heidelberg University Hospital). The RT protocol and imaging parameters are mentioned in section 3.4. The PMMA phantom was positioned via laser crosses. Small grooves on the front, as well as on the top, bottom, left and right side allow for exact alignment. Cylinder feet were pushed back as far as possible in order to reduce artifacts during scanning. Additional Beekley™ spots on the front and sides should ensure precise mapping before irradiating the phantom at HIT.

Figure 4.6 shows the placement of FNTDs (left) and Gammex insert (right) in the PMMA cylinder. The FNTD holder has a width of 6 mm and can be seen behind the white cortical bone insert. An overview of all six CT images can be found in Appendix B.2.

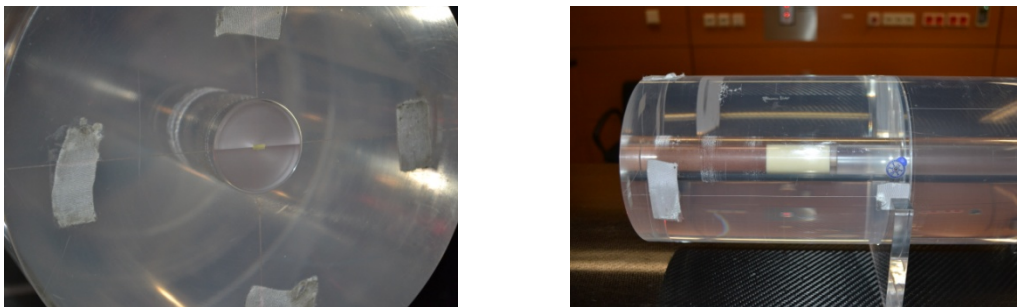


Figure 4.6 Three FNTDs in their PMMA holder (left) and combination of Gammex inserts (right)

FNTD number	insert combination
gk2002	2.8 cm PMMA, FNTDs
gk2003	16.8 cm PMMA, FNTDs
gk2004	5.6 cm PMMA, 1.0 cm titanium, 5.6 cm PMMA, FNTDs
gk2005	11.2 cm PMMA, 5.6 cm LN-450 lung, FNTDs
gk2006	5.6 cm LN-450 lung, 11.2 cm PMMA, FNTDs
gk2007	5.6 cm AP6 adipose, 5.6 cm LV1 liver, 5.6 cm CB2-30% bone, FNTDs

Table 4.2 Insert combinations behind which a holder with three FNTDs is positioned

4.2.3 Contouring and planning

Obtained DICOM data were saved to one of the standard treatment planning computers at HIT and imported to the Siemens patient system. Contouring the geometry of the experimental setup is necessary because used tissue surrogates are not listed in the Hounsfield look-up table. Therefore, the standard transformation from CT Hounsfield units to water equivalence could not be applied.

First of all, the PMMA cylinder was defined as the skin in which the dose distribution shall be calculated. Surrounding skins are always assigned “chordoma2” as biological material. After that, the inserts were marked as normal organs. Pre-defined physical materials were used to characterize their properties under irradiation. Towards the end of the contouring routine, the clinical target volume (CTV) was defined. It had a lateral area of $5 \times 5 \text{ cm}^2$ and a distal depth of 1 cm. The CTV was positioned at the center of the PMMA cylinder and had an overlap of 3 mm with the FNTDs which have not been contoured. In a final step, the laser origin and the target point were set up. They mark the center of the cylinder face and, therefore, the entrance point of the particle beam into the phantom. Note that a thin slice of air (2 mm) had to be contoured in front of the cylinder because particles can only enter air in the treatment planning software. Figure 4.7 shows the structure plan of gk2007.

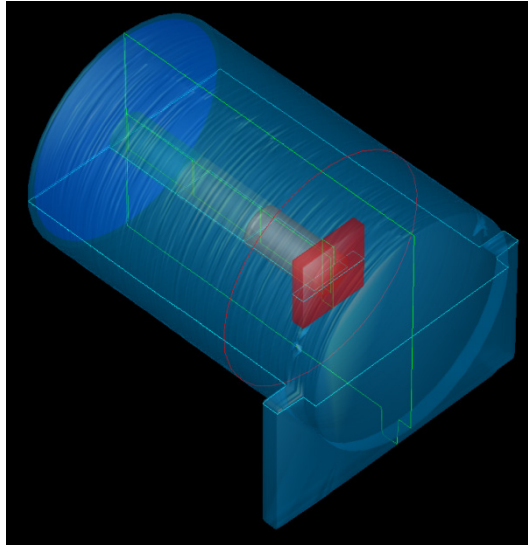


Figure 4.7 Structure plan of gk2007: PMMA cylinder in light blue containing three Gammex inserts (adipose, liver, bone) and the red CTV; air slice in dark blue at the cylinder face

Contouring and planning at HIT lead to the establishment of a workflow mentioning a detailed planning protocol, important parameters and useful hints. An excerpt can be found in appendix C.2.

Based on a complete structure plan, a treatment plan can be created. The *syngo.via* software syncs with the HIT archive and can load desired patients onto the local database. A treatment plan requires the following input parameters:

- The dose prescription defines the absorbed dose in the CTV and the number of treatment fractions.
- Incident particles, irradiation direction, lateral and longitudinal beam spot density as well as treatment room and table position must be determined under beam setup.
- The position verification menu enables x-ray positioning prior to irradiation. One can map CT scans with positioning images and apply automated alignment.
- In a final step, optimization parameters have to be set up. The standard settings for proton irradiation are mentioned in appendix C.2. They cover dose constraints, beam weights and algorithm parameters.

Once all parameters are defined, the optimization routine can be started. The computer now calculates particle energies and fluences to achieve a homogenous dose distribution in the CTV while sparing surrounding organs. This process can be repeated varying the following parameters:

- The range step influences general energy settings. For protons, a minimal value of 1.0 mm is available. The smaller the range step, the longer the total irradiation time.
- Minimal and maximal dose are given for all fractions in total. The weighting ratio decides whether the absorbed dose shall be rather over or underestimated.
- A third variable parameter is the virtual target expansion. It offers additional degrees of freedom to the optimization routine. A broad virtual target allows scan spots outside the CTV to achieve the desired dose distribution. In order to improve the distal edge, one can change the distal expansion from 2.0 (standard value) to 1.0 mm.

In an optimal depth-dose distribution, the 100% and the 10% iso-dose lines lie within the FNTD – one at the beginning and one at the end of the detector volume. This is depicted in figure 4.8.

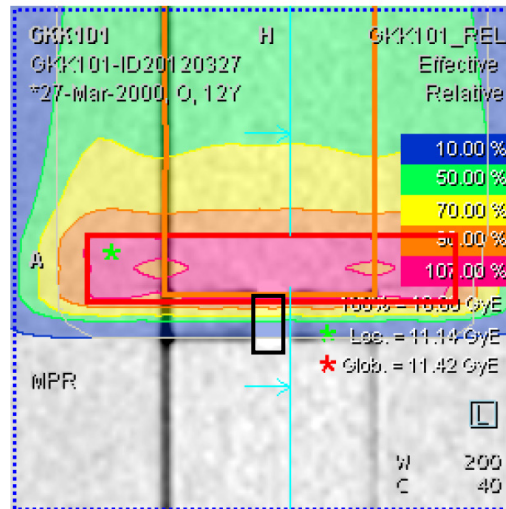


Figure 4.8

Optimized dose distribution in gk2003: The PMMA insert is contoured with the bold orange line and the CTV with the bold red line. The FNTDs appear white in the center of the image.

Figure 4.8 also shows that each optimized treatment plan was finalized calculating the effective dose distribution in the surrounding skin. The effective dose is the product of the relative biological effectiveness (RBE) with the physical absorbed dose. One finds a factor of $RBE = 1.1$ for protons.

All treatment plans had to be approved in a last step. Approval parameters are once again listed in the corresponding workflow excerpt (appendix C.2.2). The *syngo.via* software creates a treatment plan and a physical beam plan which contains the total number and exact energy of all incident protons.

4.2.4 *Irradiation at HIT*

Approved treatment plans have been enriched prior to irradiation. Laser crosses and the imager have been enabled. In the patient treatment room, the PMMA phantom was positioned by mapping the laser crosses with the grooves on the cylinder surface. The final table position was saved as reference position. Additional water tanks had to be placed on the table to ensure sufficient weight (comp. figure 4.9).



Figure 4.9 Experimental setup of the HIT irradiation

Note that laser positioning was very precise. Mapping the CT scan with x-ray images via attached Beekley™ spots was not necessary. Although being very dense, FNTDs are not well visible on the imaging projection as figure 4.10 shows.

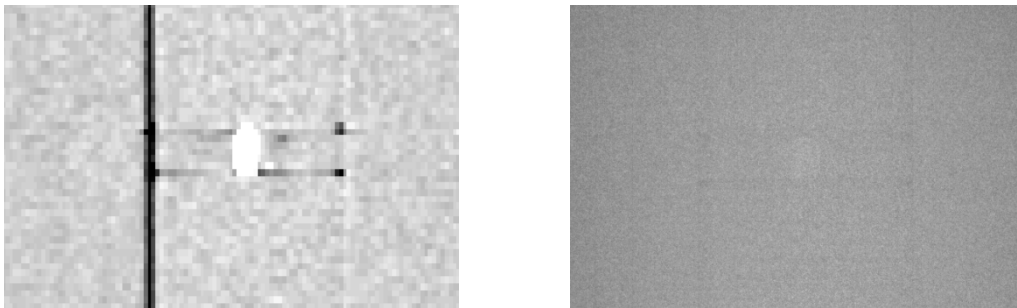


Figure 4.10 Comparison of CT image (left) and imaging projection (right)

After proton irradiation, only the inserts and the centered FNTD had to be changed. Small readjustments of the table had to be done and the next treatment plan could be applied. Unfortunately, not all FNTDs have been irradiated at the same day and in the same treatment room. Table 4.3 gives an overview of the irradiation procedure:

FNTD number	day of irradiation	treatment room
gk2002	April 4 th , 2012	H2
gk2003	April 22 nd , 2012	H1
gk2004	April 22 nd , 2012	H1
gk2005	April 26 th , 2012	H2
gk2006	April 26 th , 2012	H2
gk2007	April 26 th , 2012	H2

Table 4.3 Irradiation of the PMMA phantom at HIT

4.2.5 Detector readout

All irradiated detectors were read out with the Zeiss LSM 710 confocal microscope using the objective lens 40x / 1.4 Oil DIC II and setting the pinhole diameter to $43.6\text{ }\mu\text{m}$ (1 AU). In order to reduce acquisition time, the dwell time was set to $25.21\text{ }\mu\text{s}$. A detailed readout protocol and overview of all detectors is given in appendix B.3.



Figure 4.11 Intensity distribution in gk2002 throughout the entire detector length of 6 mm (512×512 matrix, 40% relative laser power and $100.09\text{ }\mu\text{m}$ in depth)

5 RESULTS

This chapter presents the results of the FNTD irradiation at MPI-K and HIT. In section 5.1, high-accuracy ion range measurements are performed for single tracks as well as for track bulks. The influence of the pinhole diameter on the range precision is investigated and the dose intensity correlation is analyzed over a broad range of particle fluences. Section 5.2 covers the evaluation of the in-vivo FNTD application. The predicted distal edge is compared to the actual intensity profile in the detector.

5.1 High-accuracy ion range measurements

5.1.1 Single track evaluation

Single particle tracks are well visible in detectors irradiated with fluences smaller than 10^7 cm^{-2} . By determining the entrance point into the detector and the end of the particle track one can calculate the projected range R . This evaluation technique as depicted in figure 5.1 was implemented in the FNTD readout workflow (appendix C.1).

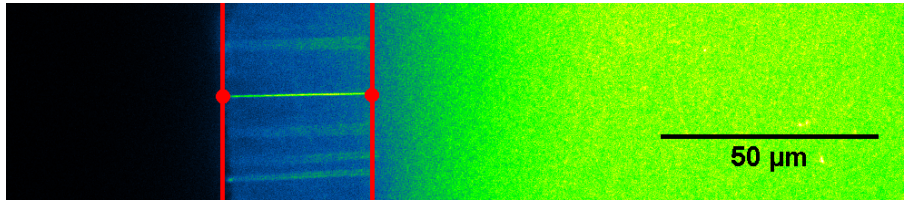


Figure 5.1 Measuring the projected range for a single particle track
(3.1×10^6 carbon ions per cm^2 at 48 MeV)

Figure 5.1 also shows that the fluorescence signal strongly decreases towards the detector edge indicating a low color center density. This means that the entrance point is not exactly identifiable. The evaluation routine could, therefore, not be automated.

In order to apply the described evaluation technique, detectors have to be irradiated exactly perpendicular to their edge. The entrance angles have been measured for a large number of particle tracks and they did not significantly differ from 90° . Measuring several hundred single tracks provided results of less than 3% deviation from the theoretical SRIM values.

FNDT no.	particle	number of analyzed tracks	measured range [μm]	SRIM range [μm]	deviation [%]
gk1000	C-12 (5+)	430	32.77 ± 0.08	33.05	0.85 ± 0.24
gk1002	S-32 (9+)	957	16.55 ± 0.04	16.27	1.72 ± 0.25
gk1003	C-12 (5+)	1354	32.59 ± 0.04	33.05	1.39 ± 0.12
gk1009	Mg-24 (8+)	225	24.28 ± 0.07	24.01	1.12 ± 0.29
jmo2000	protons	68	51.24 ± 0.39	49.78	2.93 ± 0.78
jmo2001	protons	56	162.9 ± 0.5	160.5	1.50 ± 0.31
rh3	Fe-56	36	53.11 ± 0.25	53.56	0.84 ± 0.47
rh6	Xe-132	24	49.95 ± 0.34	49.40	1.11 ± 0.69

Table 5.1 Results of the single track evaluation

FNTDs irradiated with low particles fluences at MPI-K (jmo2000 and jmo2001) as well as at the Jyväskylä Accelerator Laboratory in Finland (rh3 and rh6) have been evaluated in an internship prior to this thesis. The results are also shown in the table above and in its visualization below.

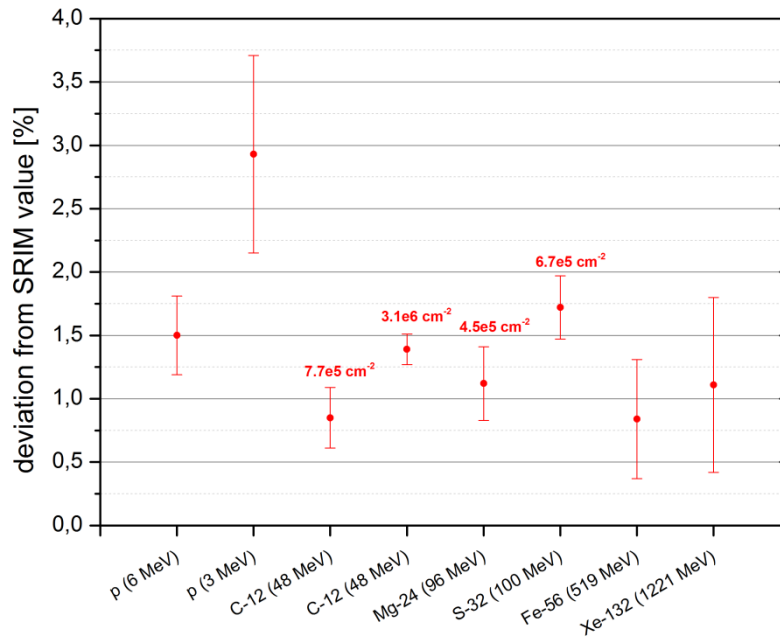


Figure 5.2 Deviations from SRIM values (single track evaluation)

5.1.2 Automated bulk evaluation

FNTDs irradiated with fluences greater than 10^7 cm^{-2} can be evaluated much more efficiently. Obtained microscope images were cut into small slices of approximately $40 \mu\text{m}$ height. The ImageJ plug-in “Stack profile Plot” by Pariksheet Nanda (2012 [15]) allows saving the gray value profile of such a slice in a .txt file. By determining the inflection points of the curve one can calculate the projected range R . This routine is illustrated in figure 5.3. Compare appendix C.1 for more details.

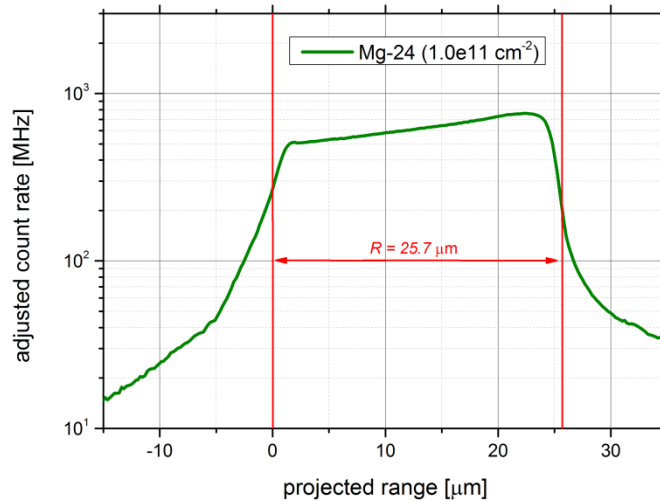


Figure 5.3 Measuring the projected range for a track bulk (1.0×10^{11} magnesium ions per cm^2 at 96 MeV)

Several hundred slices have been evaluated with this fully automated bulk evaluation routine. The results are listed in table 5.2.

FNDT no.	particle	number of analyzed slices	measured range [μm]	SRIM range [μm]	deviation [%]
gk1001	C-12 (5+)	150	34.03 ± 0.15	33.05	2.97 ± 0.45
gk1004	C-12 (5+)	170	33.13 ± 0.06	33.05	0.24 ± 0.18
gk1005	C-12 (5+)	170	32.96 ± 0.08	33.05	0.27 ± 0.24
gk1006	C-12 (5+)	250	33.64 ± 0.22	33.05	1.79 ± 0.67
gk1007	C-12 (5+)	150	35.22 ± 0.09	33.05	6.57 ± 0.27
gk1008	S-32 (9+)	100	17.23 ± 0.12	16.27	5.57 ± 0.74
gk1010	Mg-24 (8+)	150	25.99 ± 0.07	24.01	8.25 ± 0.29

Table 5.2 Results of the automated bulk evaluation

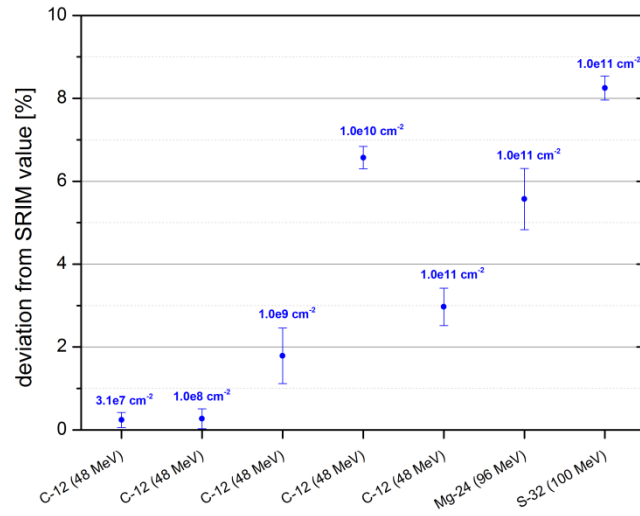


Figure 5.4 Deviations from SRIM values (track bulk evaluation)

The pinhole diameter seems to be a limiting factor for measurement precision. Fluorescent light originating outside of the focal plane washes out the detector edge. A comparison of two images only differing in pinhole diameter can be seen in figure 5.5.

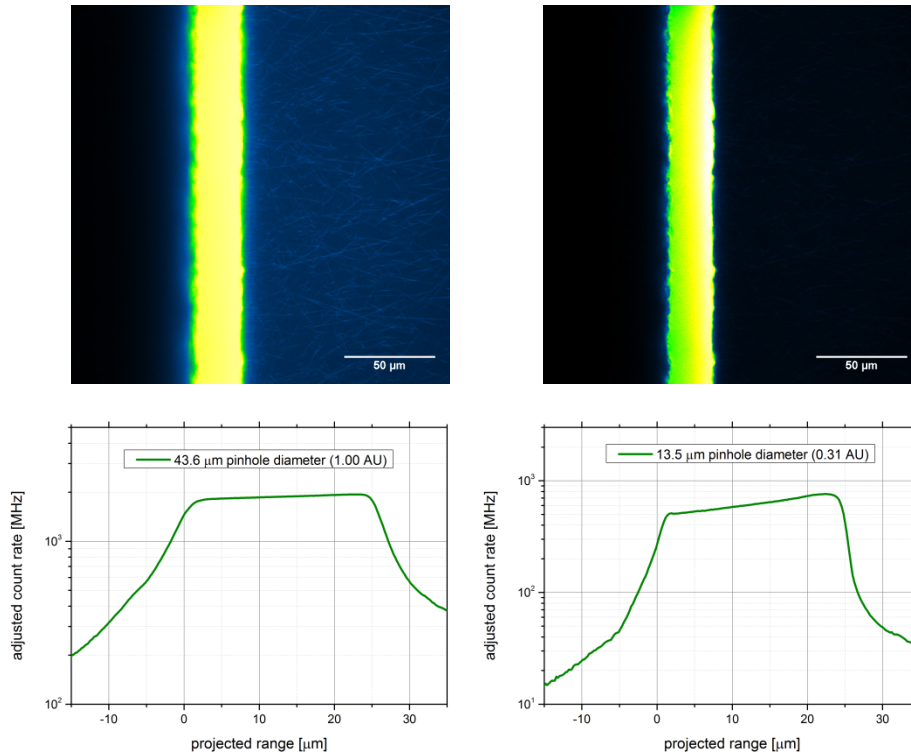


Figure 5.5 Influence of the pinhole diameter: 43.6 μm (left) and 13.5 μm (right) (1.0×10^{11} magnesium ions per cm^2 at 96 MeV)

The influence of the pinhole diameter on range accuracy is quantitatively investigated in the following section (5.1.3). The upper left image of figure 5.5 shows another interesting effect: At high fluences, nuclear interactions and fragmentation lead to the production of fast, light particles. Their tracks can be seen throughout the entire detector volume with decreasing density. Because of thin track cores and unaltered paths, they could originate from protons and neutrons. A FLUKA simulation confirmed this conclusion. Both fluences are 11 orders of magnitude smaller than the incident carbon ion fluence.

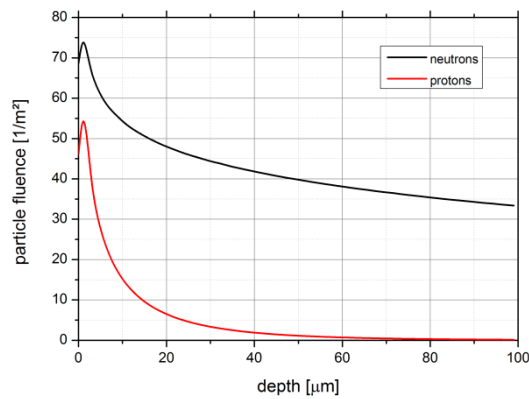


Figure 5.6 Proton and neutron fluences in a FNTD irradiated with 5.0×10^8 carbon ions per cm^2 at 48 MeV

5.1.3 Influence of pinhole diameter

FNTDs irradiated with fluences greater than 10^9 cm^{-2} show washed out detector edges when read out with the standard pinhole diameter of $43.6 \mu\text{m}$ (1 AU). The projected range has been re-measured for five different pinhole diameters (43.6 , 33.5 , 23.3 , 13.5 and $2.9 \mu\text{m}$) using automatic bulk evaluation on 50 slices. Optimal results are stated in table 5.3.

FNTD no.	particle	pinhole diameter $[\mu\text{m}]$	measured range $[\mu\text{m}]$	SRIM range $[\mu\text{m}]$	deviation [%]
gk1001	C-12 (5+)	23.3	33.23 ± 0.07	33.05	0.55 ± 0.21
gk1007	C-12 (5+)	13.5	32.14 ± 0.11	33.05	2.75 ± 0.33
gk1008	S-32 (9+)	13.5	16.31 ± 0.07	16.27	0.27 ± 0.43
gk1010	Mg-24 (8+)	13.5	24.53 ± 0.06	24.01	2.18 ± 0.25

Table 5.3 Optimal results of the pinhole variation

The reduction of the pinhole diameter can indeed improve range measurement accuracy by blocking fluorescent light from outside the focal plane. For gk1010, the deviation dropped from $(8.25 \pm 0.29)\%$ to $(2.18 \pm 0.25)\%$.

5.1.4 Summarized range results

The Zeiss LSM 710 offers a broad spectrum of readout parameters. For high-accuracy ion range measurements using FNTDs, one could comply with the following readout procedure:

- Single track evaluation ($\Phi < 10^7 \text{ cm}^{-2}$): Choose a high laser power, pixel resolution and dwell time to be able to clearly indentify the starting and end point of a track. Take multiple images in depth ($\Delta z = 3.05 \mu\text{m}$) to ensure that track cores lie in the observed focal plane. Measuring approximately 500 single tracks should lead to results of high agreement with SRIM data.
- Automatic bulk evaluation ($\Phi > 10^7 \text{ cm}^{-2}$): Set the laser power to the maximal value but ensure that APDs do not overflow. Regulate the pinhole diameter to obtain a sharp detector edge. The dwell time and pixel resolution should again be high for a good background signal ratio. Take an image along the detector edge in only one depth. The evaluation of 100 slices ($40 \mu\text{m}$ height) should yield precise results.

Following this protocol, the irradiation at MPI-K shows that FNTDs allow for measuring ion ranges with very high accuracy. Deviations from SRIM values are below the 3% threshold for all analyzed detectors.

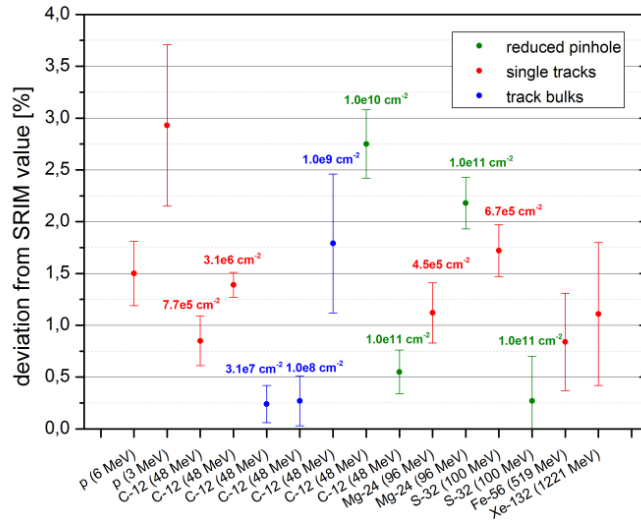


Figure 5.7

Correlation between fluence and SRIM value deviation

5.1.5 Dose intensity correlation

G. J. Sykora et al. investigated the dose response of FNTDs for fast and thermal neutrons in 2008 [21]. He comes to the conclusion that the equivalent dose is proportional to the particle fluence between 0.1 and approximately 100 mSv. Because FNTDs have been irradiated with carbon, magnesium and sulfur ions, an intensity dose calibration curve can be established for heavy charged particles.

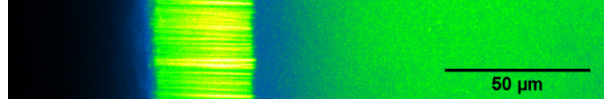


Figure 5.8 Slice of gk2005 (1.0×10^8 carbon ions per cm^2 at 48 MeV)

To do so, obtained microscope images were cut into small slices of approximately $40 \mu\text{m}$ height as depicted in figure 5.8. The program ImageJ allowed measuring the maximal intensity in each slice. In order to be able to compare the results, the same objective lens and pinhole diameter was used for the detector readout. The intensity (or total number of detected photons N), nevertheless, had to be normalized on dwell time τ and relative laser power p resulting in the adjusted count rate η :

$$\eta = \frac{N}{\tau p} [\text{MHz}] \quad (5.1)$$

By measuring η for numerous slices and taking the mean of all these values $\bar{\eta}$, detector impurities can be quantified in the standard deviation σ . In order to correlate $\bar{\eta}$ and D , one has to calculate the maximal absorbed dose in the detector volume as described in section 2.6. Figure 5.9 shows the resulting depth-dose curves based on tabulated SRIM data.

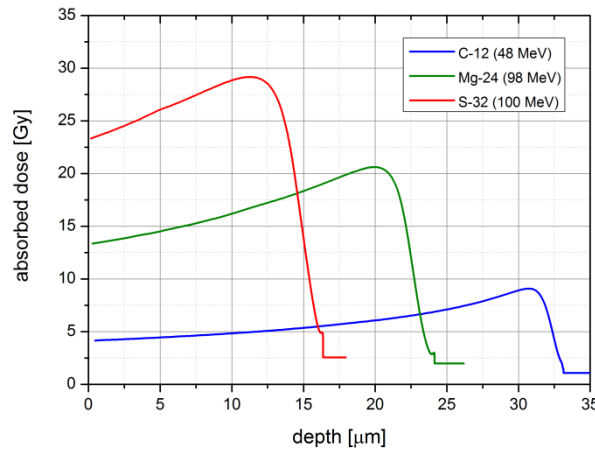


Figure 5.9 SRIM calculated depth-dose curves for 10^7 cm^{-2} carbon, magnesium and sulfur ion beams

One can now calculate maximal dose values for each irradiated FNTD and match them with observed adjusted count rates. Figure 5.10 visualizes table 5.6.

FNTD no.	particle	total kinetic energy [MeV]	particle fluence [cm ⁻²]	maximal absorbed dose [Gy]	adjusted count rate [MHz]
gk1000	C-12 (5+)	48.0	7.7×10^5	7.0×10^{-1}	3.58 ± 0.65
gk1001	C-12 (5+)	48.0	1.0×10^{11}	9.1×10^4	122 ± 9
gk1002	S-32 (9+)	100	6.7×10^5	1.9×10^0	2.48 ± 0.14
gk1003	C-12 (5+)	48.0	3.1×10^6	2.8×10^0	1.98 ± 0.14
gk1004	C-12 (5+)	48.0	3.1×10^7	2.8×10^1	2.53 ± 0.34
gk1005	C-12 (5+)	48.0	1.0×10^8	9.1×10^1	7.42 ± 0.89
gk1006	C-12 (5+)	48.0	1.0×10^9	9.1×10^2	48.3 ± 7.2
gk1007	C-12 (5+)	48.0	1.0×10^{10}	9.1×10^3	98.0 ± 1.6
gk1008	S-32 (9+)	100	1.0×10^{11}	2.9×10^5	88.5 ± 3.0
gk1009	Mg-24 (8+)	96.0	4.5×10^5	9.3×10^{-1}	1.93 ± 0.54
gk1010	Mg-24 (8+)	96.0	1.0×10^{11}	2.1×10^5	124 ± 5

Table 5.4 Correlation between maximal absorbed dose and adjusted count rate

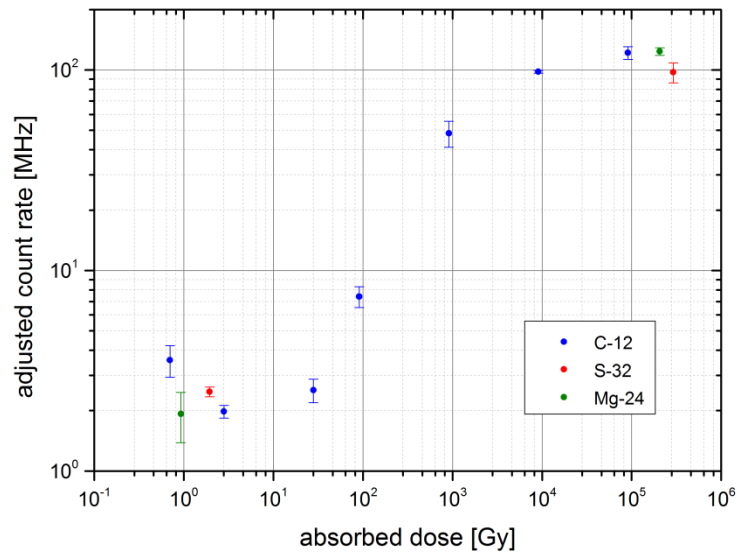


Figure 5.10 Correlation between maximal absorbed dose and adjusted count rate

The maximal absorbed dose seems to be proportional to the measured adjusted count between 20 and 1000 Gy. In his Diploma thesis (2011 [12]), Florian Lauer measured the fluorescent intensity of FNTDs after gamma irradiation. To verify the curve seen in figure 5.10, a comparison of both measurements is depicted in figure 5.11.

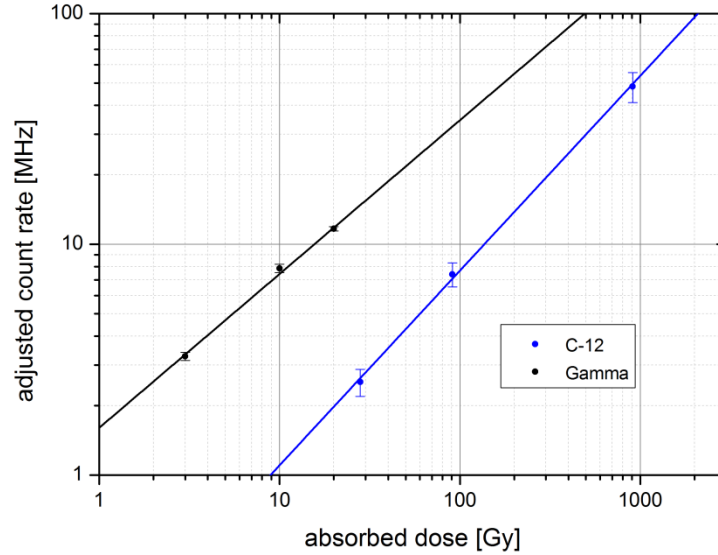


Figure 5.11 Comparison of carbon irradiated with gamma irradiated FNTDs

One can clearly see that the two linear fits mainly differ in their intersection point with the y-axis. A possible explanation is the quenching effect: HCPs ionize along their trajectories but the detected fluorescence signal is reduced (by a factor of approximately 4) due to their high LET. Secondary electrons are not only captured in color centers but also recombine with holes in the valence band effectively decreasing the density of $F_2^+(2Mg)$ color centers. Another reducing parameter could be multiple electron capture resulting in neutral $F_2(2Mg)$ color centers which are not stimulated by the red 633 nm laser line.

5.2 In-vivo range measurements

5.2.1 Distal edge comparison

Appendix B.3 shows the calculated dose distributions within the detector volume. Because FNTDs have not been contoured, the treatment planning software calculated the distal edge in PMMA and not aluminum oxide. The observed ranges should, therefore, be much shorter than the planned ones. But since the 100% and 10% iso-dose lines always lay within the detector volume, the entire fluorescent

spectrum is expected to be observed at the detector edge. The FLUKA simulation outlined in section 4.2.1 helps calculating a factor that converts the calculated dose distribution in PMMA to an equivalent dose distribution in aluminum oxide. This profile can then be compared to the observed fluorescence spectrum.

Figure 5.12 shows two simulated inverse dose profiles for 10^8 protons with a kinetic energy of 60 MeV. The left plot shows the Bragg peak in PMMA at approximately 2.65 cm depth. The right plot shows the influence on the dose distribution when placing FNTDs at 2.30 cm depth (6 mm length). The Bragg peak narrows and shifts to a smaller depth value.

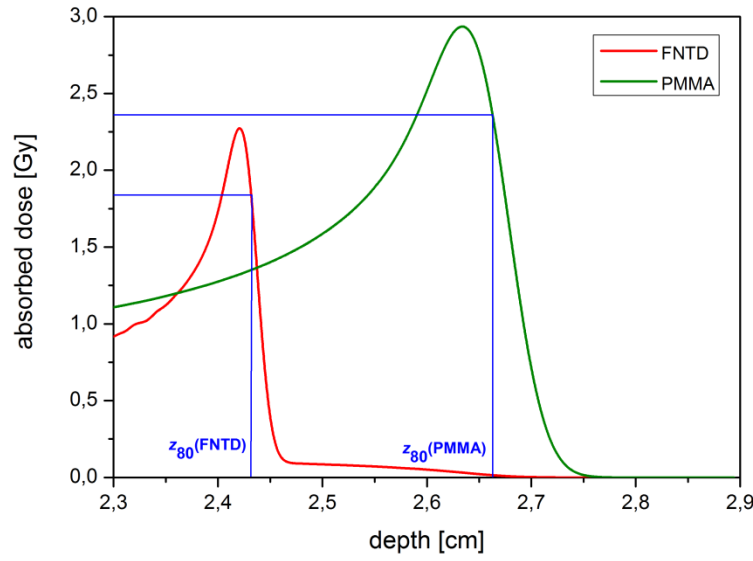


Figure 5.12 Comparison of FLUKA simulated depth-dose distributions: 60 MeV/u protons in PMMA and in aluminum oxide

The depth in which the dose drops below the 80% threshold is denoted with z_{80} . z_{FNTD} marks the beginning of the FNTD in depth (here 2.3 cm). Calculation of the conversion factor f yields:

$$f = \frac{z_{80}(\text{PMMA}) - z_{\text{FNTD}}}{z_{80}(\text{FNTD}) - z_{\text{FNTD}}} = 2.756 \quad (5.2)$$

Planned dose distributions can now be adapted:

$$z(\text{FNTD}) = \frac{z(\text{PMMA}) - z_{\text{FNTD}}}{f} + z_{\text{FNTD}} \quad (5.3)$$

Figure 5.13 shows the exemplary conversion of the planned dose distribution in gk2002 and a comparison with the observed signal profile in the detector. The 80% dose/intensity threshold marks the projected range. Appendix B.3 contains a

detailed overview of all HIT irradiated detectors and their corresponding depth-dose curves.

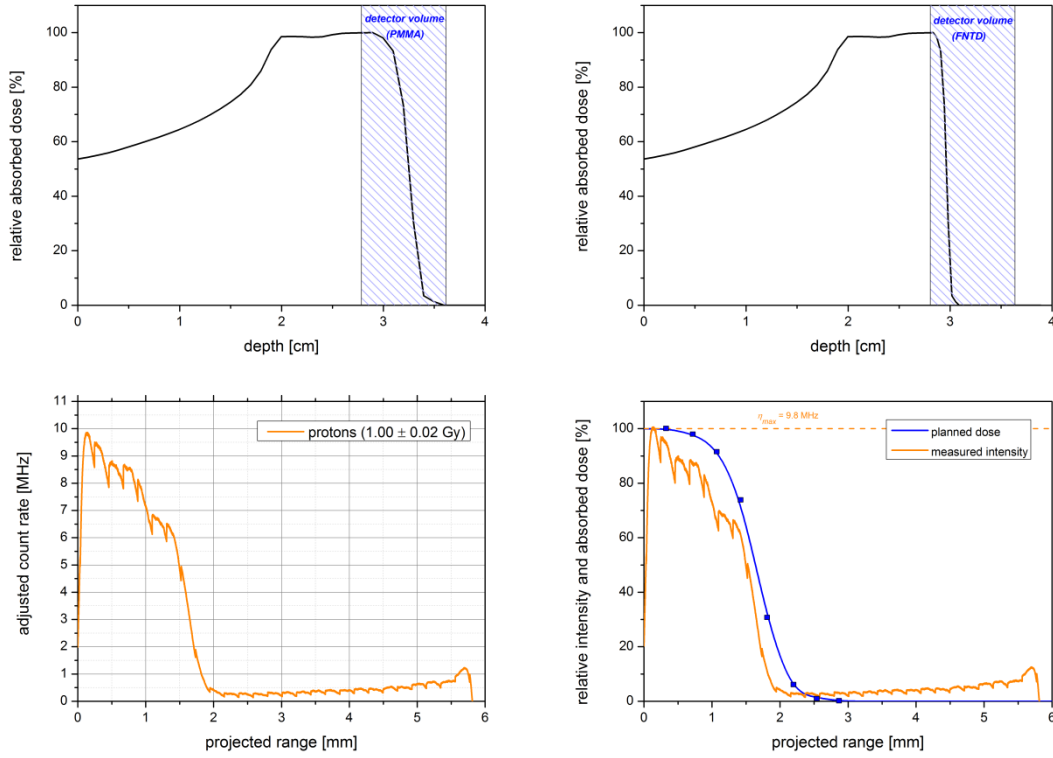


Figure 5.13 Planned depth-dose curve (top left) converted to an equivalent profile in aluminum oxide (top right); intensity profile in gk2002 (bottom left) compared to the converted dose curve (bottom right)

5.2.2 Summarized range results

Measured intensity profiles basically follow planned dose distributions in the detector volume as depicted in appendix B.3. The dips in the profiles are due to microscope vignetting. The differences in expected and monitored range lie well below the 1 mm threshold (comp. table 5.5 and figure 5.14). This threshold is defined by the CT slice thickness which is a measure for FNTD positioning accuracy. Another error influencing factor is the simulated conversion factor which may not apply entirely to each the experimental setup.

FNDT no.	particle	planned mean dose [Gy]	converted planned range [mm]	measured range [mm]	difference [mm]
gk2002	protons	1.00 ± 0.02	1.30	0.93	0.37
gk2003	protons	0.99 ± 0.02	0.87	0.54	0.33
gk2004	protons	0.97 ± 0.04	1.08	0.39	0.69
gk2005	protons	0.98 ± 0.03	0.78	0.61	0.17
gk2006	protons	0.97 ± 0.03	0.80	0.60	0.20
gk2007	protons	0.97 ± 0.04	1.07	0.65	0.42

Table 5.5 Results of the in-vivo range measurements

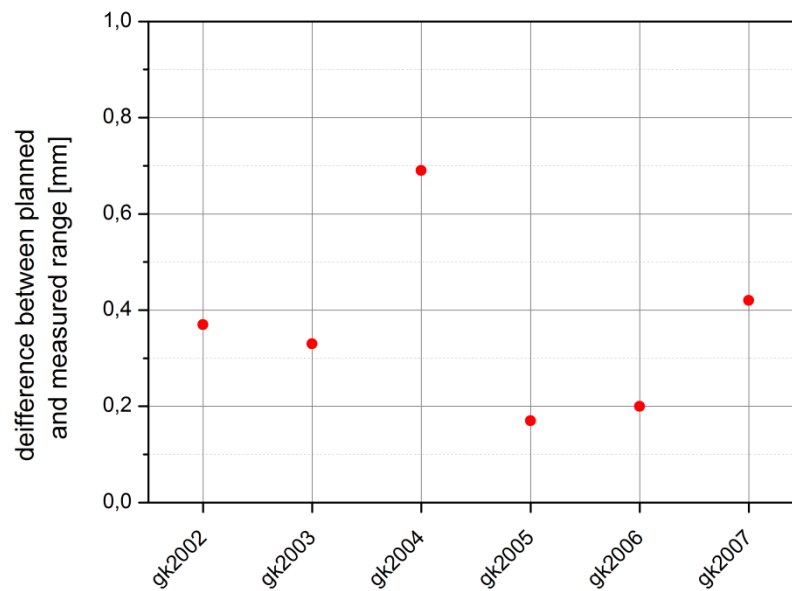


Figure 5.14 Deviations from treatment planned ranges

6 DISCUSSION AND OUTLOOK

In this thesis, high-accuracy ion range measurements were performed for mono-energetic particle beams using single track as well as track bulk evaluation techniques. FNTDs have also been irradiated under clinical conditions in order to investigate the basic suitability for clinical in-vivo applications. The distal edge predicted by the treatment plan was compared to the actual intensity profile detected. This chapter discusses the findings and suggests further experiments.

6.1 Range measurements based on single track evaluation

6.1.1 *Results of the single track evaluation*

In the single track evaluation routine introduced in section 5.1.1, entrance and end point are marked individually for each particle track. Being very time consuming, this routine, nevertheless, allows for measuring the projected range (and the lateral straggling) with less than 3% deviation of theoretical SRIM values. Table 5.1 shows that measured ranges both over- and under-estimate the projected range. A systematic dependency on energy or particle type could, therefore, not be found. A reason for these statistical residuals could be the low fluorescence intensity at the detector edge leading to uncertainties in determining the entrance point into the detector. Furthermore, FNTD edges are not cut perfectly straight with fluctuations up to 2 μm . Combination of these two circumstances might explain observed deviations.

6.1.2 *Influence of the nuclear stopping power component*

The spatial resolution of FNTDs cannot be the reason for the residuals found since structures on a submicrometer-scale can be resolved. Because radiochromatic transformation is believed to be triggered by electronic interactions in the detector, the influence of the linear nuclear stopping power component on the projected range is analyzed in figure 6.1. Comparison of electronic and nuclear contributions to the SRIM calculated depth-dose curve of a 48 MeV carbon ion beam in aluminum oxide, nevertheless, show that the latter can be neglected when measuring the projected range at the 80% dose threshold. Even at very low particle energies, nuclear interactions have little influence on the depth-dose curve. The assumption

that they are not being monitored by FNTDs can, therefore, not explain 3% deviations from tabulated SRIM values.

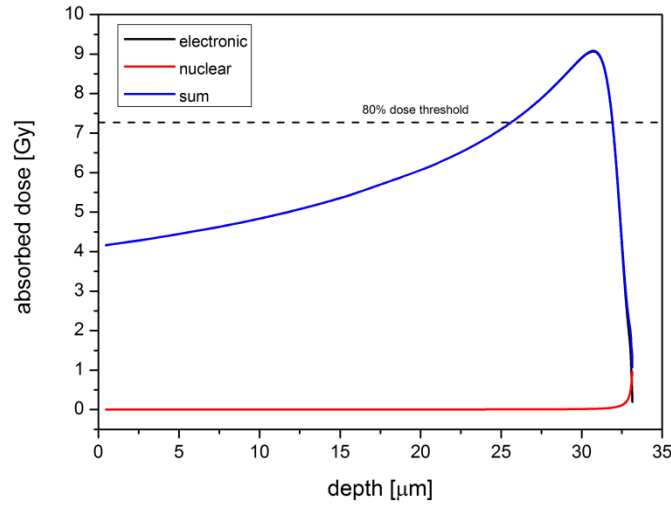


Figure 6.1 Electronic and nuclear contributions to the absorbed dose (48 MeV carbon ion beam in aluminum oxide)

Single track evaluation could be applied to detectors irradiated with fluences smaller than 10^7 cm^{-2} . This corresponds to maximal clinical doses of approximately 0.1 and 4.2 Gy for 4 MeV/u protons and carbon ions, respectively.

6.2 Range measurements based on automated bulk evaluation

6.2.1 Results of the track bulk evaluation

For FNTDs irradiated with more than 10^7 particles per cm^2 , range measurement routines could be automated. The fast bulk evaluation technique determines the distance between two inflection points in the corresponding intensity profile yielding the same level of precision (less than 3% deviation of theoretical SRIM data). A limiting factor is the pinhole diameter. Fluorescent light originating outside of the focal plane washes out the detector edge. It was shown that the reduction of the pinhole diameter can indeed improve range measurement accuracy for high particle fluences by blocking fluorescence off focus.

6.2.2 Quenching effect

In contrast to a simple picture, the observed quenching effect can be separated into saturation within a single track core and saturation of the entire detector due to

high particle fluences. The comparison of carbon irradiated with gamma irradiated FNTDs clearly shows saturation effects within HCP track cores (comp. figure 5.11). The detected fluorescent signal is reduced due to a high LET. The adjusted count rate, nevertheless, increases linearly with increasing dose up to 1000 Gy (10^9 carbon ions per cm^2 at 48 MeV). This shows that clinical particle fluences will not cause additional saturation effects in FNTDs.

6.3 In-vivo range measurements

6.3.1 Results of the in-vivo range measurements

In a second series of experiments, FNTDs placed behind various insert combinations have been irradiated with protons under clinical conditions. Measured intensity profiles agree with planned dose distributions within limiting CT resolution. The possible high range measurement accuracy enabled by FNTDs is, nevertheless, jeopardized by positioning difficulties due to the CT slice thickness of 1 mm. Standard CT scans are even done with a slice thickness of 3 mm which is large compared to a FNTD length of 6 mm (~ 20 mm water equivalent). Another factor influencing planned dose distributions is the water equivalent path length (WEPL) of used tissue surrogates. If the treatment planning software contains errors concerning these values, the true projected range will of course differ from calculation.

Figure 6.2 shows that FNTDs are not only suitable for range measurements but also for monitoring entire predicted dose distributions. The planned dose plateau from 3 to 4 mm depth is reproduced by the fluorescence profile. The intensity peak at the end of the detector might originate from transition effects.

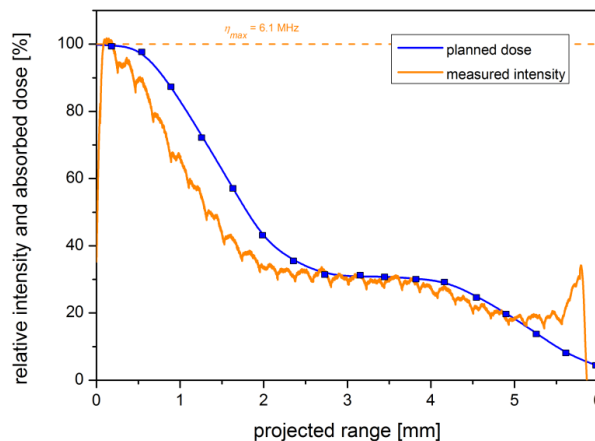


Figure 6.2

Comparison of measured intensity profile with converted planned dose distribution

6.3.2 WEPL measurements

The WEPLs of individual PMMA and aluminum oxide slabs have recently been measured with 270.55 MeV/u carbon ions (C. Tremmel, pers. comm.):

$$\text{WEPL}(\text{PMMA}) = 1.154 \quad (6.1)$$

$$\text{WEPL}(\text{FNTD}) = 3.288 \quad (6.2)$$

Note that the treatment planning system assumes a PMMA WEPL of 1.165. Based on these results, the conversion factor should be slightly larger than the one introduced in equation 5.2:

$$f = \frac{\text{WEPL}(\text{FNTD})}{\text{WEPL}(\text{PMMA})} = 2.849 > 2.756 \quad (6.3)$$

Although the experimental setup does not match the in-vivo FNTD irradiation with approximately 60 MeV/u protons and one could question the concept of a constant WEPL over a broad energy range, the fact that measured ranges are smaller than the prediction (comp. table 5.5) allows concluding that the conversion factor f might have been slightly under-estimated.

All FNTDs irradiated within this thesis were aligned parallel to the beam direction in order to assure that particle tracks and track bulks are parallel to the focal planes of the microscope. This ensures that projected ranges are not being under-estimated. But because precisely parallel irradiation cannot always be assured in in-vivo FNTD applications, the following further experiments are being suggested.

6.4 Suggestions for further experiments

6.4.1 In-vivo irradiation under pre-clinical conditions

Described and analyzed in-vivo irradiations of FNTDs faced a large number of uncertainties (e.g. CT imaging resolution, optimization routine, beam quality, broad energy spectrum). One could repeat the in-vivo experiments with a mono-energetic proton beam breaking down the level of complexity. High range conformity could be achieved leading to a very sharp distal edge in the detector volume. This would additionally simplify the comparison of the forward calculated treatment plan with the detected fluorescence profile.

6.4.2 *In-vivo irradiation with carbon ions*

At HIT, patients can be treated with protons as well as with carbon ions. One could, therefore, repeat the outlined in-vivo irradiation with a carbon ion beam. Additional high resolution CT scans would minimize FNTD positioning uncertainties. A second holder could ensure the investigation of tilted irradiated as it would be the case in most in-vivo FNTD applications.

6.4.3 *Dose calibration curves for protons and carbon ions*

The irradiation of FNTDs over a broad range of fluences has shown that the fluorescent signal strength is proportional to the absorbed dose in a HCP dependent dose regime. One could, therefore, establish calibrations curves for protons and carbon ions by irradiating FNTDs with ion beams of well-known energy and fluence. By correlating adjusted count rate and absorbed dose, one could validate calculated treatment plans without FNTD positioning constraints. This might open the possibility for FNTD applications in quality assurance and irradiation control.

APPENDIX

A LISTS

A.1 List of abbreviations (in alphabetical order)

APD	Avalanche photodiode
CERN	European Organization for Nuclear Research
CSDA	Continuous slowing down approximation
CT	Computed tomography
CTV	Clinical target volume
DKFZ	German Cancer Research Center
FLUKA	Fluctuating cascade
FNTD	Fluorescent nuclear track detector
HCP	Heavy charged particles
HIT	Heidelberg Ion-Beam Therapy Center
ICRU	International Commission on Radiation Units and Measurements
INFN	National Institute for Nuclear Physics, Italy
LET	Linear energy transfer
LSM	Laser scanning microscopy
MPI-K	Max Planck Institute for Nuclear Physics
PET	Positron emission tomography
PMMA	Polymethyl methacrylate
PMT	Photomultiplier
RBE	Relative biological effectiveness
SRIM	Stopping and Range of Ions in Matter
WEPL	Water equivalent path length

A.2 List of symbols (as mentioned in the text)

$\text{Al}_2\text{O}_3:\text{C, Mg}$	Aluminum oxide doped with carbon and magnesium
Φ	Particle fluence
\vec{r}	Point vector in space
N	Number of particles
A_{\perp}	Perpendicular area
ϵ_i	Deposited energy in a single interaction
ϵ_{in}	Kinetic energy of an incident ionizing particle
ϵ_{out}	Sum of the kinetic energies of all ionizing particles leaving the interaction
Q	Change in the rest energies of the nucleus and of all particles involved in the interaction
ϵ	Total imparted energy
m	Rest mass
D	Absorbed dose
E	Kinetic energy
l	Traversed distance
S	Linear stopping power
S_{el}	Linear electronic stopping power
S_{rad}	Linear radiative stopping power
S_{nuc}	Linear nuclear stopping power
LET_{Δ}	Linear energy transfer
Δ	Specific energy cutoff for secondary electrons

E_{Δ}^{δ}	Sum of the kinetic energies of all secondary electrons greater than Δ
R	Projected range and outer cylinder radius
E_{min}	Minimal kinetic energy
E_{max}	Maximal kinetic energy
ΔR_n	Width of voxel n
E_n	Kinetic energy when entering voxel n
S_n	Corresponding linear stopping power to E_n
E_0	Initial kinetic energy of the particle beam
D_n	Absorbed dose in voxel n
ρ	Physical density
D_{max}	Maximal absorbed dose
$F_2^{2+}(2Mg)$	Two-electron color center
τ	Lifetime and dwell time
E_g	Band gap
δ_z	Effective slice thickness
d	Pinhole diameter
η_{max}	Maximal photon counting rate
g	Digital gain
Δg	Digital offset
l_x, l_y	Field size
p	Relative excitation laser power
Δz	Step size in depth
N_{max}	Maximal dynamic range
L	Cylinder length
r	Inner cylinder radius
ρ_e	Electron density
ρ_e^w	Electron density of water
I	Faraday cup current
z	Charge of incident particles

η	Adjusted count rate
$\bar{\eta}$	Mean adjusted count rate
σ	Standard deviation
z_{80}	Depth is which the absorbed dose reaches the 80% threshold
z_{FNTD}	Beginning of FNTD in depth
f	Conversion factor

A.3 List of figures

Figure 2.1	CSDA for particles traversing small volumes of width ΔR_n
Figure 2.2	SRIM calculated depth-dose curve of a 100 MeV/u carbon ion beam in PMMA
Figure 2.3	FLUKA simulated depth-dose curve of a 100 MeV/u carbon ion beam in PMMA
Figure 3.1	Size of a FNTD compared to a one cent coin
Figure 3.2	Crystal structure of corundum (α -Al ₂ O ₃)
Figure 3.3	Model of the F ₂ ²⁺ (2Mg) aggregate defect
Figure 3.4	Absorption and fluorescence of F ₂ ²⁺ (2Mg) and F ₂ ⁺ (2Mg) color centers
Figure 3.5	Schematic diagram of the Zeiss LSM 710 light path
Figure 3.6	Schematic diagram of the PMMA cylinder
Figure 3.7	Gammex inserts: adipose, lung, cortical bone and liver
Figure 4.1	FNTD being placed on position 8
Figure 4.2	Schematic diagram of the Faraday cup

Figure 4.3	3.1×10^6 carbon ions per cm^2 with track cores on and off focus	Figure 5.7	Correlation between fluence and SRIM value deviation
Figure 4.4	Schematic diagram of the FNTD irradiation at HIT	Figure 5.8	Slice of gk2005 (1.0×10^8 carbon ions per cm^2 at 48 MeV)
Figure 4.5	FLUKA simulated two dimensional depth-dose distribution	Figure 5.9	SRIM calculated depth-dose curves for 10^7 cm^{-2} carbon, magnesium and sulfur ion beams
Figure 4.6	Three FNTDs in their PMMA holder (left) and combination of Gammex inserts (right)	Figure 5.10	Correlation between maximal absorbed dose and adjusted count rate
Figure 4.7	Structure plan of gk2007	Figure 5.11	Comparison of HCP irradiated with gamma irradiated FNTDs
Figure 4.8	Optimized dose distribution in gk2003	Figure 5.12	Comparison of FLUKA simulated depth-dose distributions: 60 MeV/u protons in PMMA and in aluminum oxide
Figure 4.9	Experimental setup of the HIT irradiation	Figure 5.13	Planned depth-dose curve (top left) converted to an equivalent profile in aluminum oxide (top right); intensity profile in gk2002 (bottom left) compared to the converted dose curve (bottom right)
Figure 4.10	Comparison of the CT image (left) and the imaging projection (right)	Figure 5.14	Deviations from treatment planned ranges
Figure 4.11	Intensity distribution in gk2002 throughout the entire detector length of 6 mm	Figure 6.1	Electronic and nuclear contributions to the absorbed dose (48 MeV carbon ion beam in aluminum oxide)
Figure 5.1	Measuring the projected range for a single particle track (3.1×10^6 carbon ions per cm^2 at 48 MeV)	Figure 6.2	Comparison of measured intensity profile with converted planned dose distribution
Figure 5.2	Deviations from SRIM values (single track evaluation)		
Figure 5.3	Measuring the projected range for a track bulk (1.0×10^{11} magnesium ions per cm^2 at 96 MeV)		
Figure 5.4	Deviations from SRIM values (track bulk evaluation)		
Figure 5.5	Influence of the pinhole diameter: 43.6 μm (left) and 13.5 μm (right) (1.0×10^{11} magnesium ions per cm^2 at 96 MeV)		
Figure 5.6	Proton and neutron fluences in a FNTD irradiated with 5.0×10^8 carbon ions per cm^2 at 48 MeV		

A.4 List of tables

Table 3.1	Excitation and emission bands of Al_2O_3 : C, Mg crystals
Table 3.2	Physical and electron densities of Gammex inserts
Table 4.1	MPI-K irradiation protocol
Table 4.2	Insert combination behind which a holder with three FNTDs is positioned
Table 4.3	Irradiation of the PMMA phantom at HIT
Table 5.1	Results of the single track evaluation
Table 5.2	Results of the automated bulk evaluation
Table 5.3	Optimal results of the pinhole variation
Table 5.4	Correlation between maximal absorbed dose and adjusted count rate
Table 5.5	Results of the in-vivo range measurements

A.5 List of experiments

February 28 th , 2012	Irradiation of FNTDs with carbon and sulfur ions (detectors gk1000 – gk1008) at MPI-K
February 29 th , 2012	Irradiation of FNTDs with magnesium ions (detectors gk1009 and gk1010) at MPI-K
March 29 th , 2012	CT scans of all six insert combinations at the Kopfklinik, Heidelberg University Hospital on Siemens SOMATOM Sensation 4 CT Scanner
March 30 th , 2012	Contouring and planning at HIT (in corporation with Swantje Ecker)
April 4 th , 2012	Irradiation of gk2002 with protons at HIT (patient room H2)
April 11 th – 13 th , 2012	Contouring and planning at HIT (in corporation with Swantje Ecker)
April 22 nd , 2012	Irradiation of gk2003 and gk2004 with protons at HIT (patient room H1)
April 26 th , 2012	Irradiation of gk2005, gk2006 and gk2007 with protons at HIT (patient room H2)

B READOUT PROTOCOLS AND IMAGES

B.1 FNTDs irradiated at MPI-K

The following images were obtained using the objective lens 40x / 1.4 Oil DIC II and setting the pinhole diameter to 43.6 μm (1 AU).

FNDT no.	particle	kinetic energy [MeV]	fluence [1/cm ²]	digital gain and dwell time [μs]	matrix size [px and μm]	tile scan size [matrices]	surface, step size, range [μm], slice no.	laser intensity [%]
gk1000	C-12	48.0	7.7×10^5	0.21, 50.42	512×512 , 212.1×212.1	1×3	55.94, 3.05, 100.65, 34	100
gk1001	C-12	48.0	1.0×10^{11}	0.20, 50.42	512×512 , 212.1×212.1	1×18	65.21, <i>no stack</i>	15
gk1002	S-32	100	6.7×10^5	0.20, 78.79	164×512 , 112.8×353.6	1×3	63.02, 3.05, 100.65, 34	100
gk1003	C-12	48.0	3.1×10^6	0.20, 67.53	192×508 , 119.6×317.4	1×2	43.60, 3.05, 100.65, 34	100
gk1004	C-12	48.0	3.1×10^7	0.20, 64.65	200×512 , 82.6×212.1	1×1	47.05, 3.05, 100.65, 34	100
gk1005	C-12	48.0	1.0×10^8	0.20, 57.96	223×512 , 92.0×211.8	1×1	34.56, 3.05, 100.65, 34	100
gk1006	C-12	48.0	1.0×10^9	0.20, 50.42	512×512 , 212.1×212.1	1×18	61.06, 10, 20, 3	30
gk1007	C-12	48.0	1.0×10^{10}	0.20, 50.42	512×512 , 212.1×212.1	1×18	57.29, <i>no stack</i>	20
gk1008	S-32	100	1.0×10^{11}	0.20, 50.42	512×512 , 212.1×212.1	1×18	71.17, <i>no stack</i>	20
gk1009	Mg-24	96.0	4.5×10^5	0.20, 63.56	204×519 , 84.1×214.7	1×3	50.47, 3.05, 100.65, 34	100
gk1010	Mg-24	96.0	1.0×10^{11}	0.20, 50.42	512×512 , 212.1×212.1	1×18	77.88, <i>no stack</i>	15

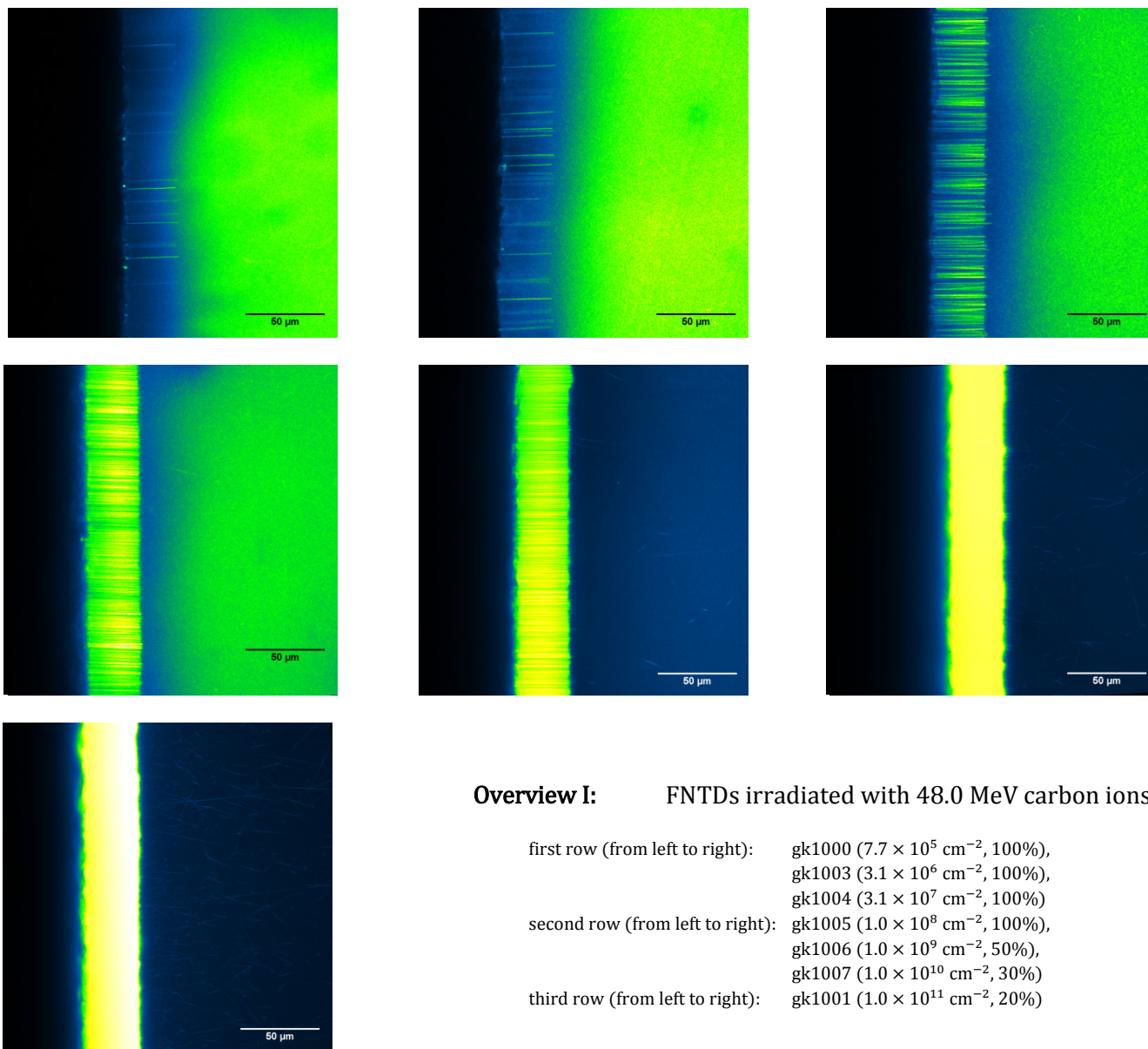
The following three sets of images were obtained using the objective lens 40x / 1.4 Oil DIC II at five different pinhole diameters (43.6, 33.5, 23.3, 13.5 and 2.90 μm).

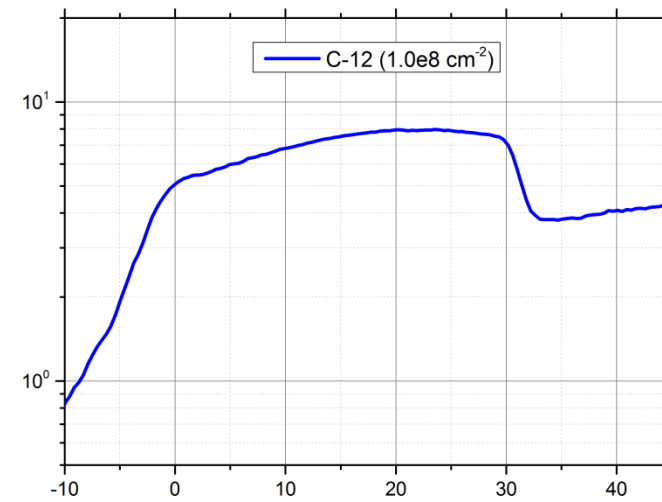
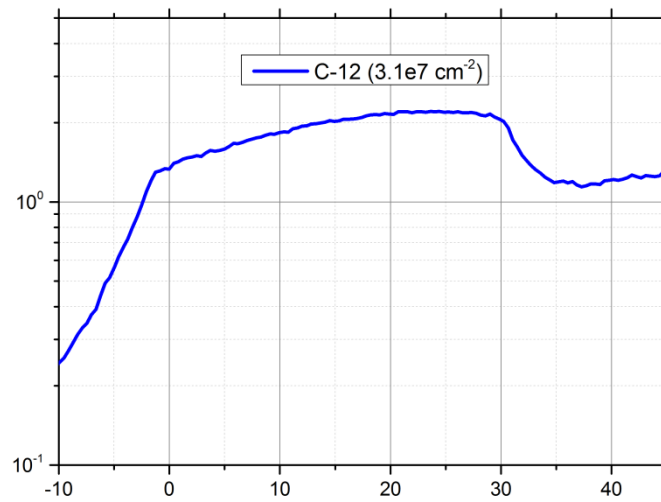
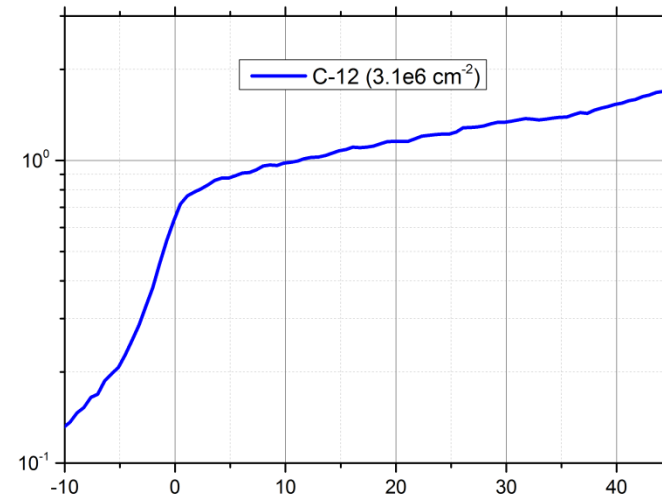
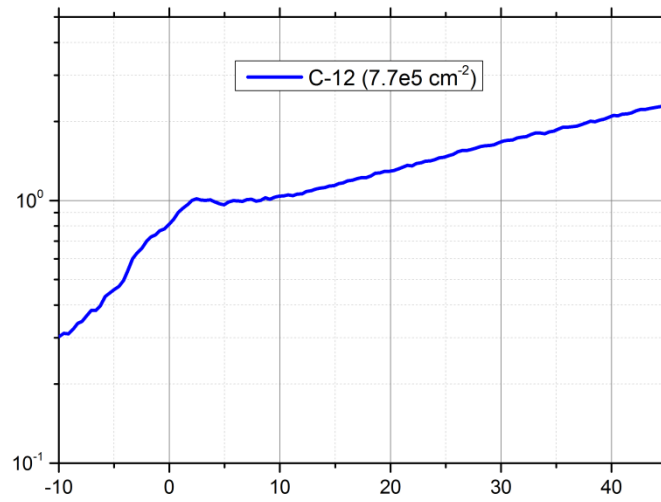
FNDT no.	particle	kinetic energy [MeV]	fluence [$1/\text{cm}^2$]	digital gain and dwell time [μs]	matrix size [px and μm]	tile scan size [matrices]	surface, step size, range [μm], slice no.	laser intensity [%]
gk1001	C-12	48.0	1.0×10^{11}	0.20, 50.42	512×512 , 212.1×212.1	1×10	107.31, <i>no stack</i>	15
gk1008	S-32	100	1.0×10^{11}	0.20, 50.42	512×512 , 212.1×212.1	1×10	178.16, <i>no stack</i>	20
gk1010	Mg-24	96.0	1.0×10^{11}	0.20, 50.42	512×512 , 212.1×212.1	1×10	109.82, <i>no stack</i>	15

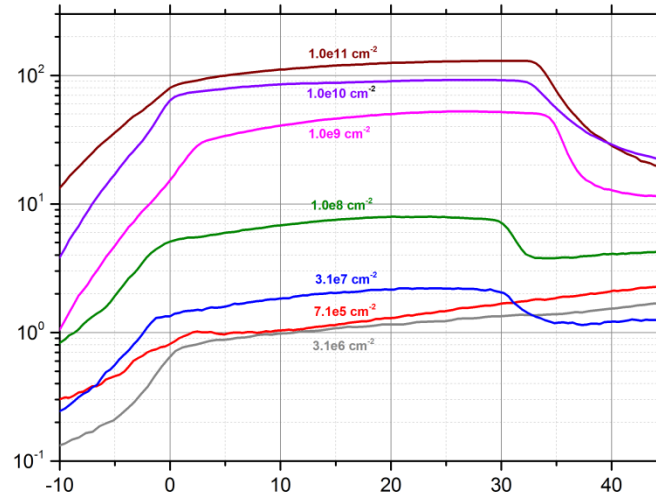
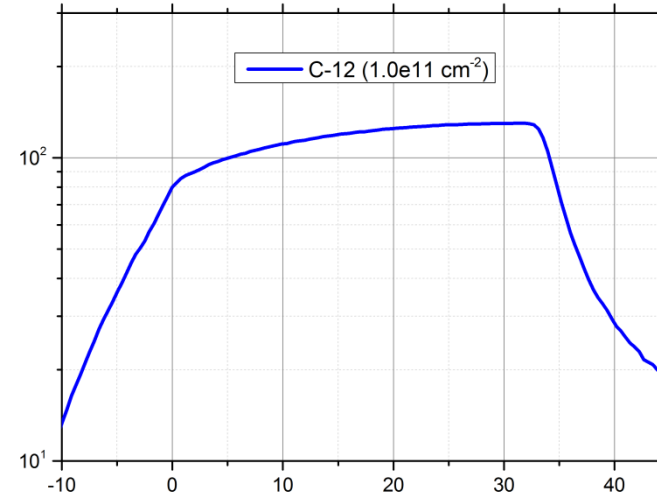
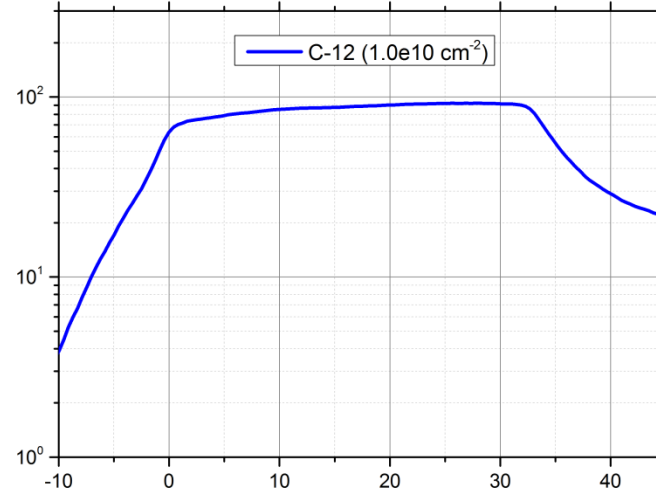
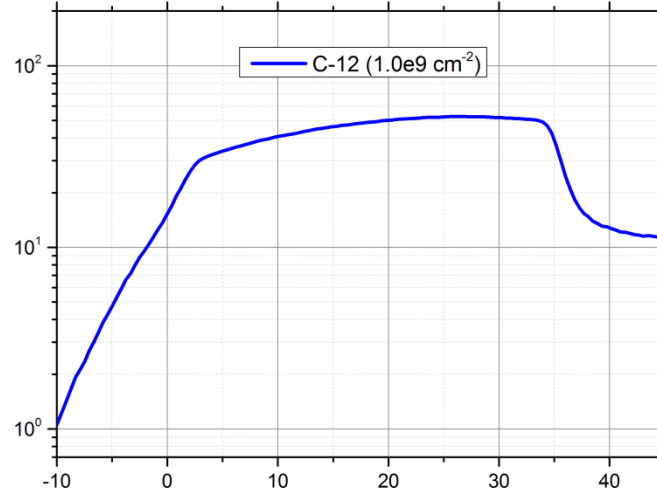
The following set of images was obtained using the objective lens 40x / 1.4 Oil DIC II at a pinhole diameter of 13.5 μm (0.31 AU) and five different relative laser powers (25, 40, 60, 80 and 100%).

FNDT no.	particle	kinetic energy [MeV]	fluence [$1/\text{cm}^2$]	digital gain and dwell time [μs]	matrix size [px and μm]	tile scan size [matrices]	surface, step size, range [μm], slice no.	laser intensity [%]
gk1010	Mg-24	96.0	1.0×10^{11}	0.20, 50.42, 1	512×512 , 212.1×212.1	---	109.82, <i>no stack</i>	25, 40, 60, 80, 100

The following images for overview purposes were obtained using the objective lens 40x / 1.4 Oil DIC II at a dwell time of 100.85 μs :



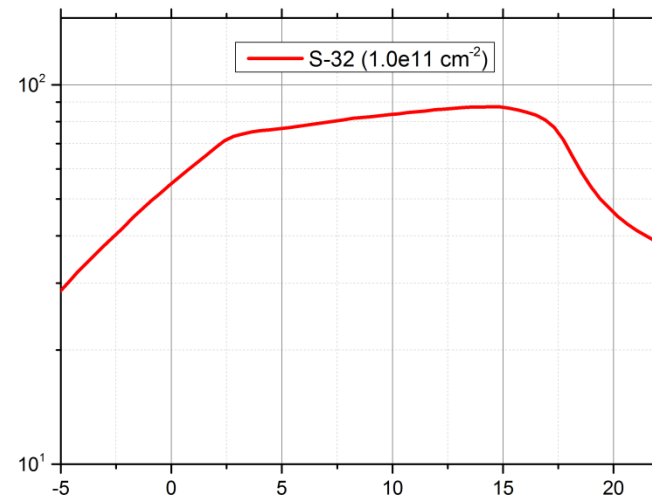
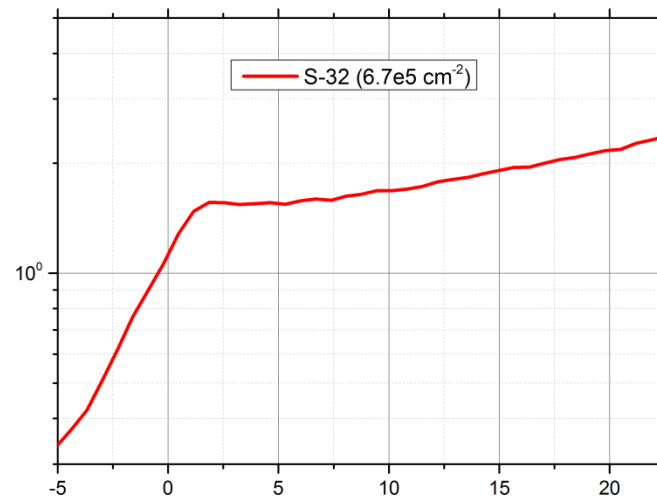
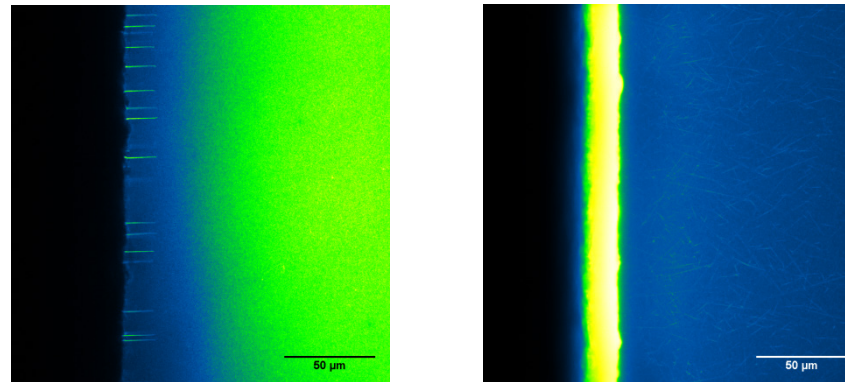




Corresponding intensity profiles for FNTDs irradiated with carbon ions:
adjusted count rate [MHZ] plotted against detector depth [μm]

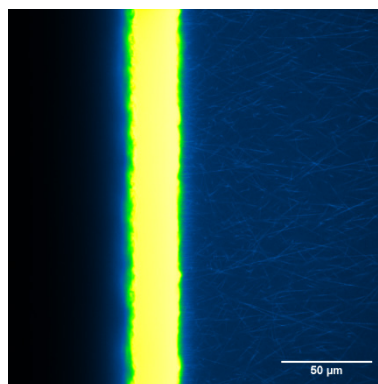
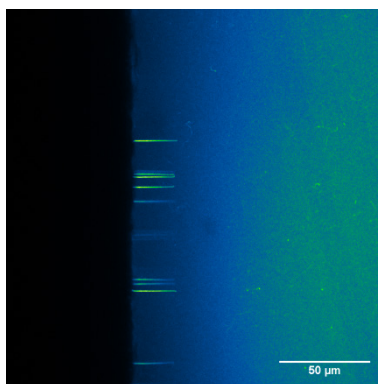
Overview II: FNTDs irradiated with
100 MeV sulfur ions

left: gk1002 ($6.7 \times 10^5 \text{ cm}^{-2}$, 100%)
right: gk1008 ($1.0 \times 10^{11} \text{ cm}^{-2}$, 20%)



**Corresponding
intensity profiles for
FNTDs irradiated with
sulfur ions:**

adjusted count rate
[MHZ] plotted against
detector depth [μm]

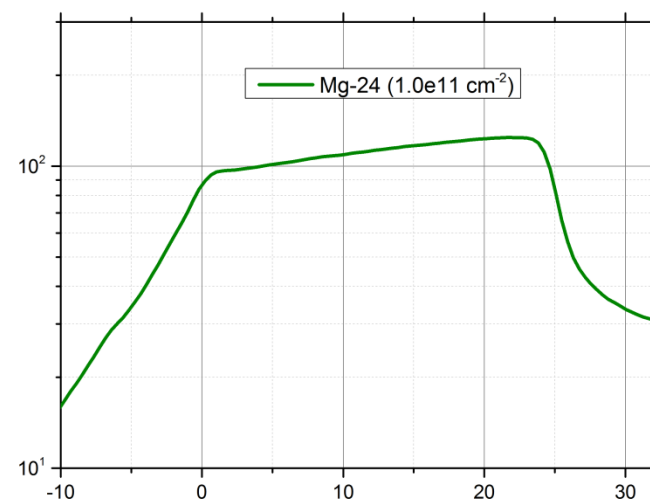
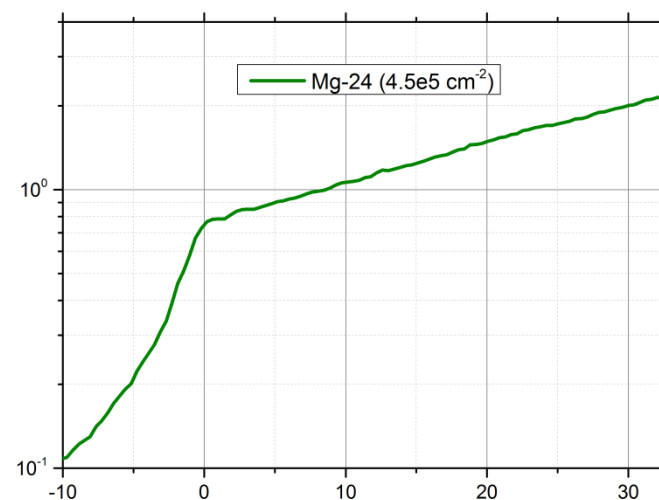


Overview III: FNTDs irradiated with 96.0 MeV magnesium ions

left: gk1009 ($4.5 \times 10^5 \text{ cm}^{-2}$, 100%)
 right: gk1010 ($1.0 \times 10^{11} \text{ cm}^{-2}$, 30%)

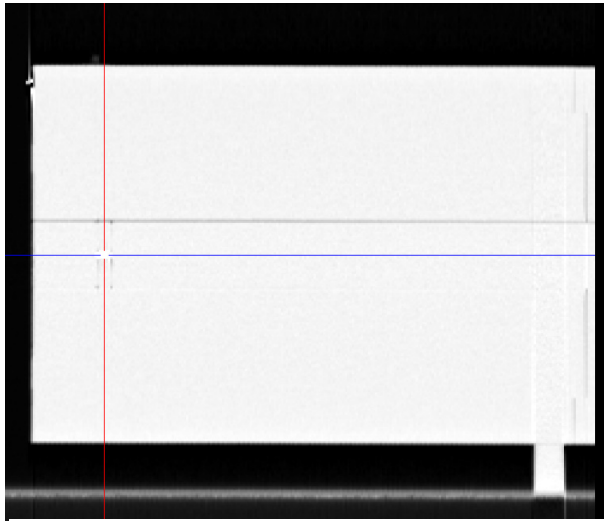
Corresponding intensity profiles for FNTDs irradiated with magnesium ions:

adjusted count rate [MHZ] plotted against detector depth [μm]



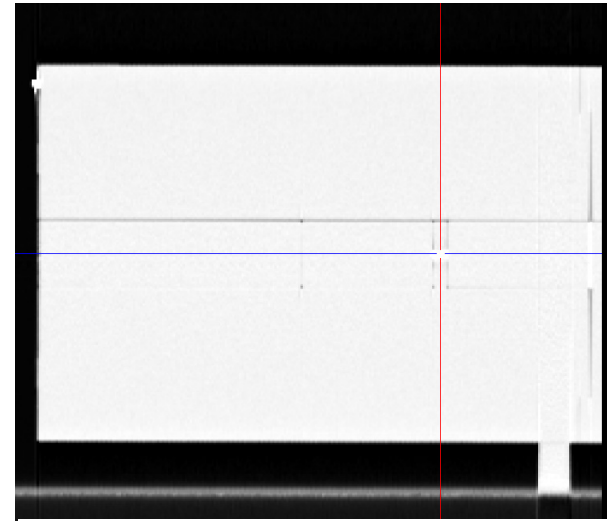
B.2 CT images of the PMMA phantom

Obtained DICOM (Digital Imaging and Communications in Medicine) data were visualized with the open-source software MITK-3M3 (version 1.1) developed by the division of Medical and Biological Informatics at DKFZ and mint medical. The intersection of the blue and red line marks the position of the FNTDs. In all following images, protons would enter the PMMA cylinder from the left.



gk2002:

2.8 cm PMMA in front of the FNTD holder

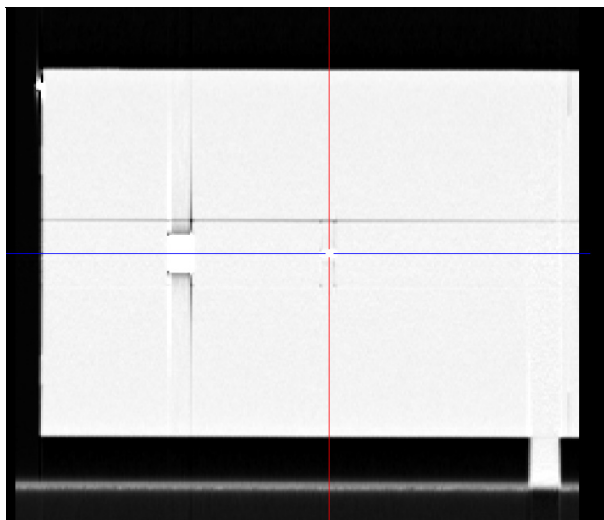


gk2003:

16.8 cm PMMA in front of the FNTD holder

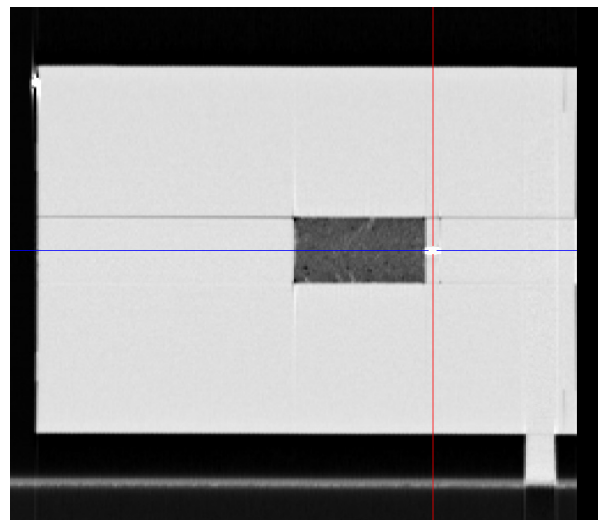
gk2004:

5.6 cm PMMA, 1.0
cm titanium and
5.6 cm PMMA in
front of the FNTD
holder



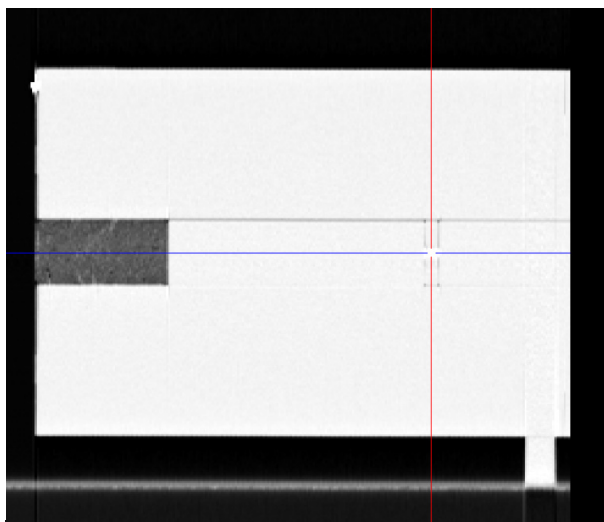
gk2005:

11.2 cm PMMA
and 5.6 cm LN-450
lung in front of the
FNTD holder



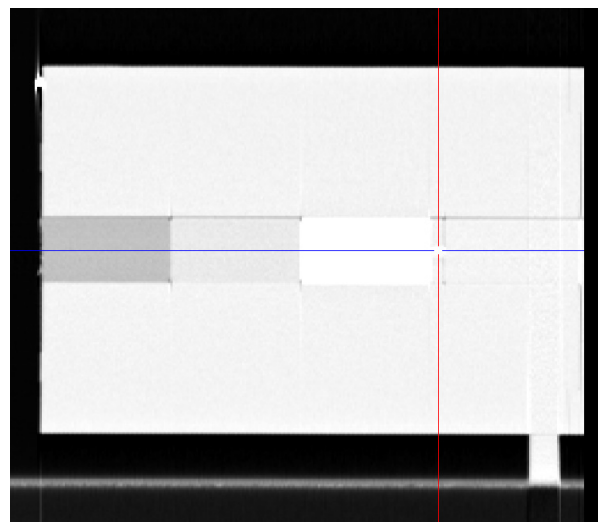
gk2006:

5.6 cm LN-450
lung and 5.6 cm
PMMA in front of
the FNTD holder



gk2007:

5.6 cm AP6
adipose, 5.6 cm
LV1 liver and 5.6 cm
CB2-30% bone
in front of the
FNTD holder

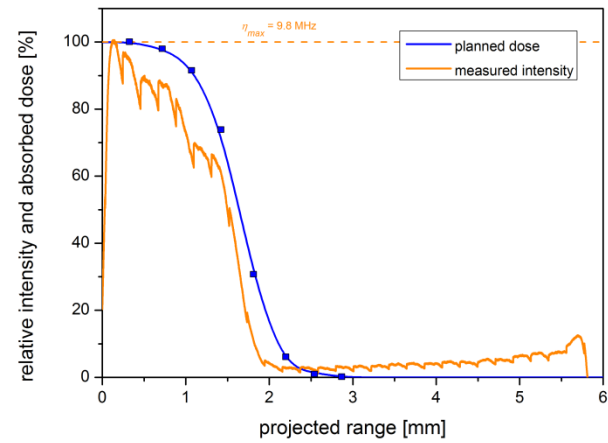
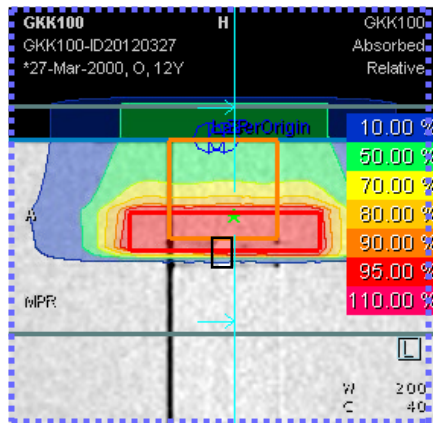


B.3 FNTDs irradiated at HIT

The following images were obtained using the objective lens 40x / 1.4 Oil DIC II and setting the pinhole diameter to 43.6 μm (1 AU). They show the intensity distribution throughout the entire detector length of 6 mm at a depth of approximately 100 μm .

FNDT no.	particle	prescribed mean dose [Gy]	digital gain and dwell time [μs]	matrix size [px and μm]	tile scan size [matrices]	surface, step size, range [μm], slice no.	laser intensity [%]
gk2002	protons	1.00 ± 0.02	0.20, 25.21	512×512 , 212.1×212.1	6×29	100.09, <i>no stack</i>	40
gk2002	protons	0.99 ± 0.02	0.20, 25.21	512×512 , 212.1×212.1	6×29	100.09, <i>no stack</i>	60
gk2002	protons	0.97 ± 0.04	0.20, 25.21	512×512 , 212.1×212.1	6×29	100.09, <i>no stack</i>	60
gk2002	protons	0.98 ± 0.03	0.20, 25.21	512×512 , 212.1×212.1	6×29	100.09, <i>no stack</i>	60
gk2002	protons	0.97 ± 0.03	0.20, 25.21	512×512 , 212.1×212.1	6×29	100.09, <i>no stack</i>	60
gk2002	protons	0.97 ± 0.04	0.20, 25.21	512×512 , 212.1×212.1	6×29	100.09, <i>no stack</i>	60

The intensity profiles are being compared to the optimized dose distributions calculated with the *syngo.via* software. By applying the conversion factor f , PMMA calculated distal edges have been transformed to aluminum oxide equivalent curves. Because of the CT slice thickness, there only is one data point each converted mm.

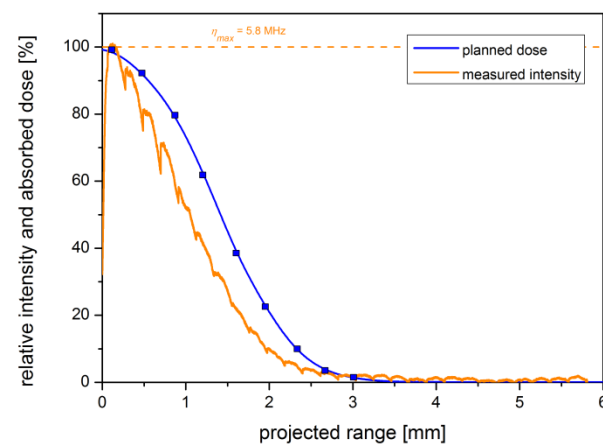
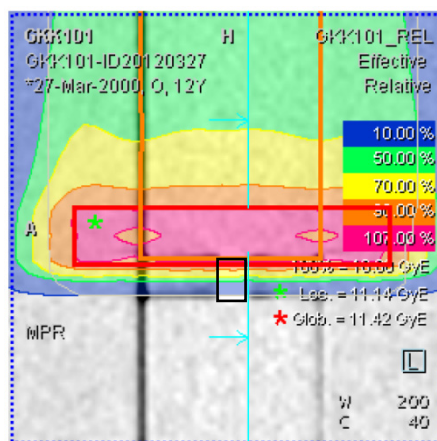


gk2002:

top: 2.8 cm PMMA in front of the FNTD (40% laser intensity)

bottom left: planned dose distribution with FNTD in black rectangle

bottom right: comparison of measured intensity profile with converted planned dose distribution

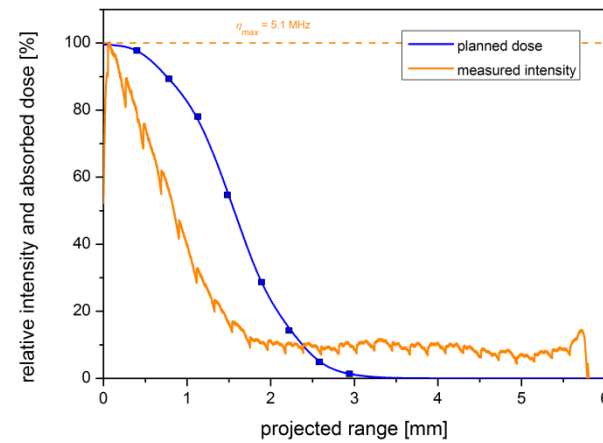
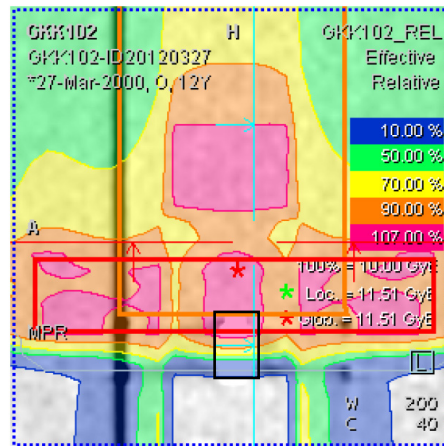
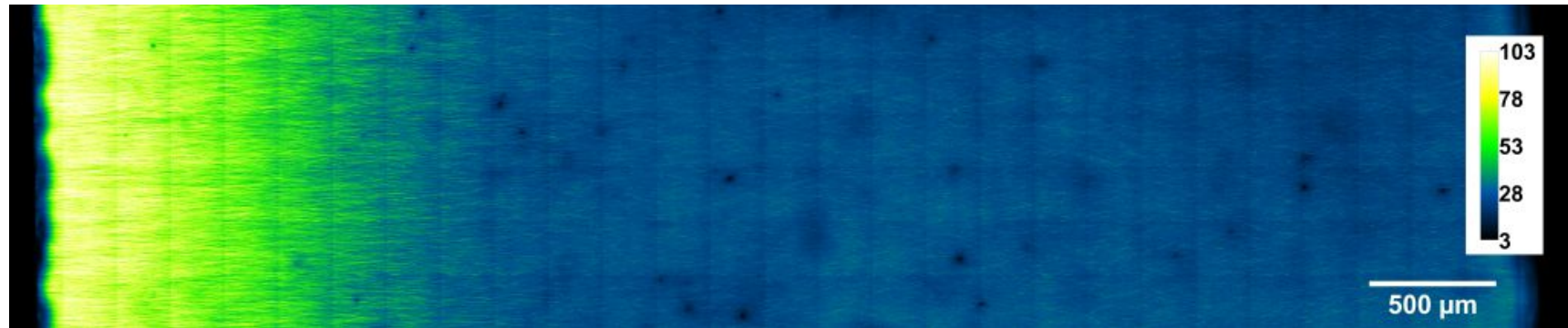


gk2003:

top: 16.8 cm PMMA in front of the FNTD (60% laser intensity)

bottom left: planned dose distribution with FNTD in black rectangle

bottom right: comparison of measured intensity profile with converted planned dose distribution

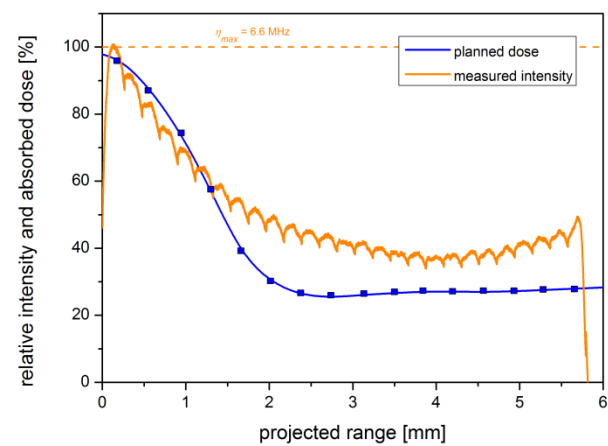
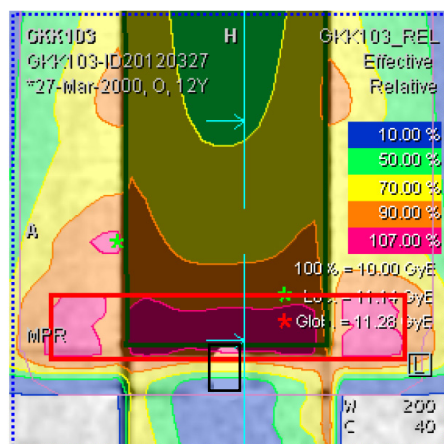
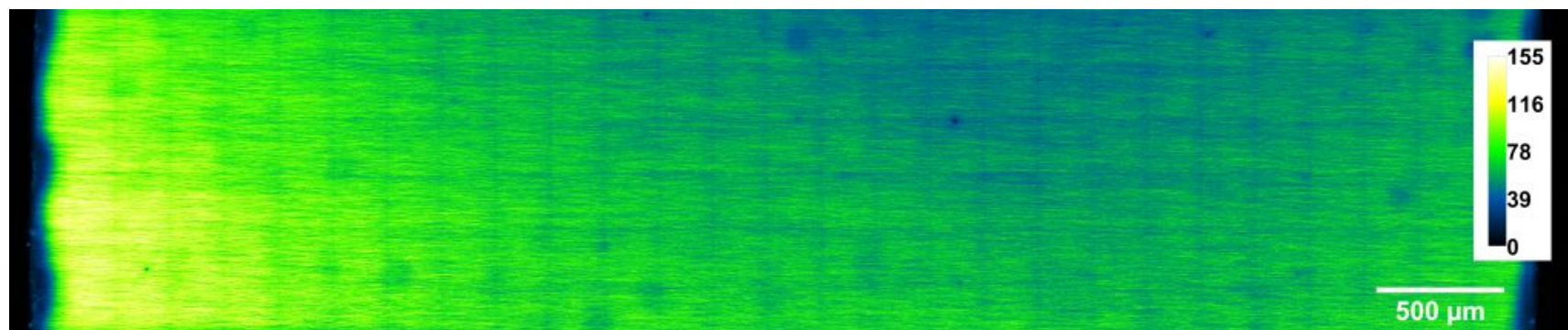


gk2004:

top: 5.6 cm PMMA, 1.0cm titanium and 5.6 cm PMMA in front of the FNTD (60% laser intensity)

bottom left: planned dose distribution with FNTD in black rectangle

bottom right: comparison of measured intensity profile with converted planned dose distribution

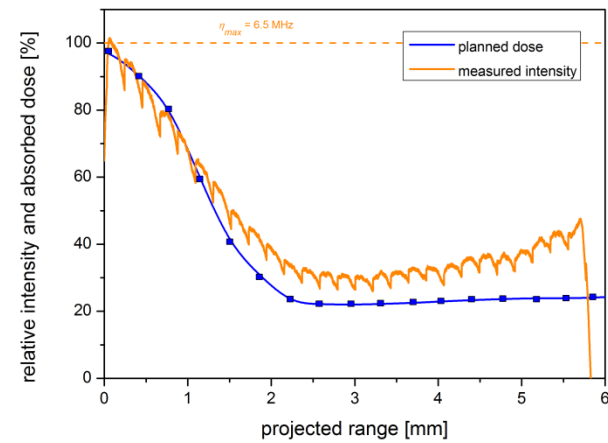
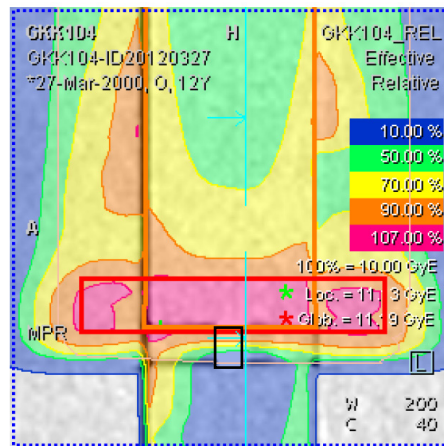
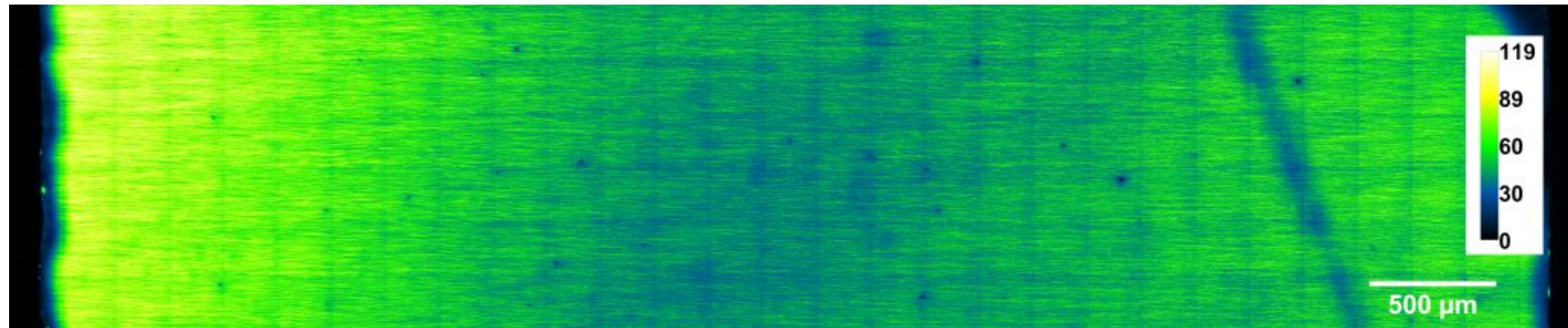


gk2005:

top: 11.2 cm PMMA and 5.6 cm LN-450 lung in front of the FNTD (60% laser intensity)

bottom left: planned dose distribution with FNTD in black rectangle

bottom right: comparison of measured intensity profile with converted planned dose distribution

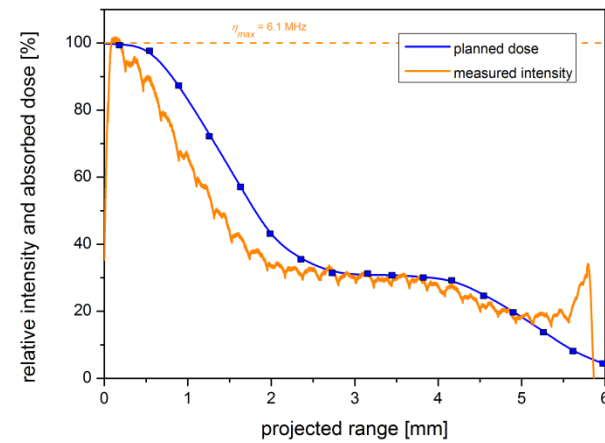
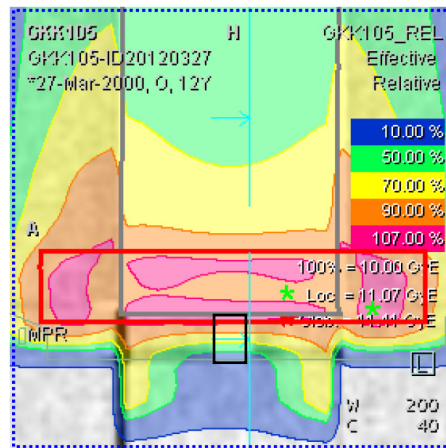
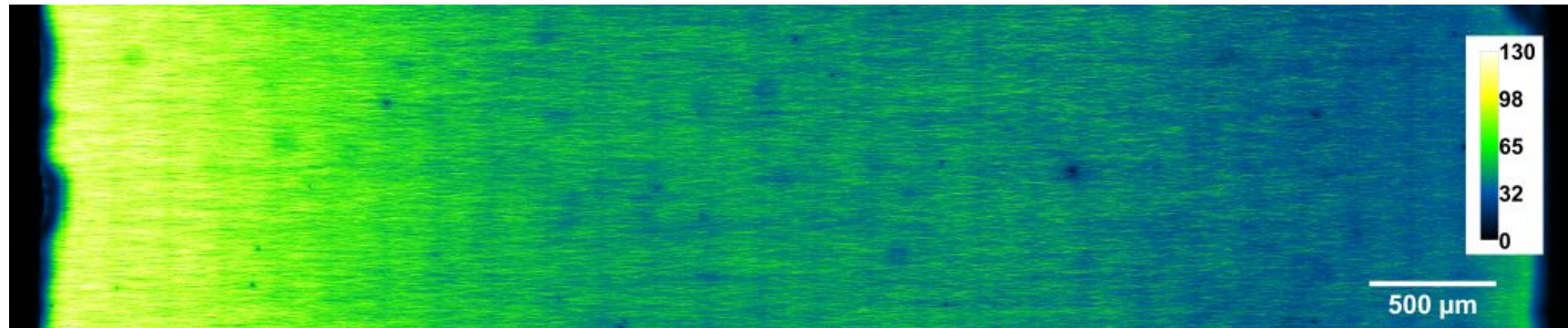


gk2006:

top: 5.6 cm LN-450 lung and
11.2 cm PMMA in front of the
FNTD (60% laser intensity)

bottom left: planned dose
distribution with FNTD in
black rectangle

bottom right: comparison of
measured intensity profile
with converted planned dose
distribution



gk2007:

top: 5.6 cm AP6 adipose, 5.6 cm LV1 liver and 5.6 cm CB2-30% bone in front of the FNTD (60% laser intensity)

bottom left: planned dose distribution with FNTD in black rectangle

bottom right: comparison of measured intensity profile with converted planned dose distribution

C WORKFLOW EXCERPTS

C.1 FNTD range measurements in ImageJ

1. Load image in ImageJ.
 2. Scale is automatically set when you open .ism files.
 3. Label slices of the z-stack to get a better overview.
 - Image -> Stacks -> Label
 - Format = 0
 - Starting value = Δz_{First} of the z-stack
 - Interval = Δz of the z-stack
 - Text = FNTD number: particle, energy, fluence
 - Select *Use text tool font*, so the text is written the way you chose it before and is the same for all z-stacks you work with.
 - Select *Preview* to adjust font size and arrange text location.
 4. To get a better contrast select another color and adjust the brightness. Play around with these setting to clearly see the edge of the detector.
 - Image -> Lookup tables -> Green Fire Blue (optional)
 - Image -> Adjust -> Brightness/Contrast
 5. Since you can see the same track on multiple slices of the z-stack, choose that slice for range measurement, where the track is most exact.
 6. In order to measure the range (horizontal length of the track) of a specific track, follow the following steps.
 - Use the *Straight Line Selection Tool* from the Toolbar
 - Hold the shift-key during drawing the line, because the shift-key forces the line to be horizontal.
 - Analyze -> Measure (Ctrl + M) will show you the results (length, ...)
 - Analyze -> Label will make your selected line permanent + labels it with a number
- alternative method:
- Use the *Multi-Point Tool* from the Toolbar
 - Select the starting point of the track.
 - Select the end point of the track.
 - Analyze -> Measure (Ctrl + M) will show you the x and y positions of the two points. Label the track (Analyze -> Label).

- The difference Δx is the range of the particle.
- 7. In order to measure the range (horizontal length) of a bulk of tracks by hand (fluences $> 1e7 \text{ 1/cm}^2$), follow the following steps.
 - Image setup:
 - Straighten your image by setting the line width (Edit -> Options -> Line Width) to approximately 150% of the expected range and selecting the center of the bulk on top and bottom of your image. Edit -> Selection -> Straighten will now generate a modified image. This tool also works for stacks when editing the first image.
 - Image -> Transform -> Rotate 90 Degrees Right will restore the original image/stack orientation.
 - If you are working with a stack you will now have to montage it: Image -> Stacks -> Make Montage. (Columns = 1, Rows = no. of images in stack, Scale Factor = 1).
 - Image -> Stacks -> Tools -> Montage to Stack will cut up your montage in a desired number of pieces and arrange them in a new stack.
 - There are now two different methods allowing the measurement of the bulk range.
 - Use the *Rectangle Tool* from the Toolbar:
 - Analyze -> Measurements... Check "Bounding rectangle"
 - Select an area in which the starting and end point of numerous tracks are identifiable.
 - Analyze -> Measure (Ctrl + M) will show you the width (and height) of the drawn rectangle in pixels.
 - Repeat this routine for all images in your stack.
 - Use *Plot Profile* from the Toolbar:
 - Select all (Ctrl + A)
 - Analyze -> Plot Profile (Ctrl + K)
 - Select the rise and fall of the gray value using the multi-point tool.
 - Measure the x positions (in pixels) of your two selected points (Ctrl + M).
 - Repeat this routine for all images in your stack.
- 8. The bulk range measurement for fluences $> 1e7 \text{ 1/cm}^2$ can also be performed automatically for high resolution images with a sharp detector edge:
 - Setup your image following the instructions under 7.
 - Add *Stack profile Plot* macro (by Pariksheet Nanda) to your StartupMacros.txt file under /Program Files/ ImageJ/macros:
 - Select all (Ctrl + A) of your montaged stack.

- Run the *Stack profile Plot* macro.
 - The text file containing gray value information of all images in your stack will be saved to your desktop.
- Evaluation in R:
 - Find the maximal and minimal slope of each profile. The difference of these positions is the projected range in pixel units.
9. In order to measure the real length of a specific track, follow the following steps.
- Use the *Segmented Line Selection Tool* from the Toolbar

- Create a segmented line selection by repeatedly clicking with the mouse on the track. Each click will define a new line segment. Double click when finished.
- Analyze -> Measure will show you the results (length,...)
- Analyze -> Label will make your selected line permanent + labels it with a number

10. Optionally:

- Maybe it is helpful to draw a vertical line, where the edge of the FNTD is expected to be. It might be helpful to better see the starting point of the track during the actual range measurement.

C.2 Treatment planning at HIT

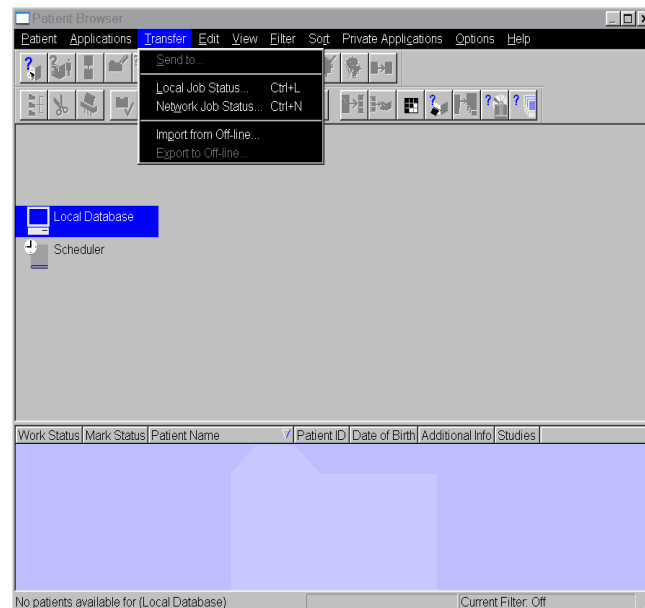
C.2.1 Contouring on Siemens patient system

- save the obtained CT data to
\\10.7.72.26\transfer\data\TPS-FileSharing\MyFolder
- using one of the treatment planning computers copy all CT images to C:\TEMP\MyFolder
- data import (set switch on VC):
 - open the patient browser with “, Entf” on the keyboard
 - transfer -> import from off-line... -> select all CT images of the corresponding scan
 - a new patient will open under local database

- drag the imported files onto the contouring window (see screenshot 1)
- contouring:
 - add new structure
 - for PMMA select normal organ as type, PMMA as physical material and <not assigned> as biological material (color can also be adjusted)
 - for surrounding skin (area where dose will be calculated in the treatment plan) select external as type, <not assigned> as physical



- material and chordoma2 as biological material
- for target volume select CTV as type, <not assigned> as physical and biological material



screenshot 1: patient browser

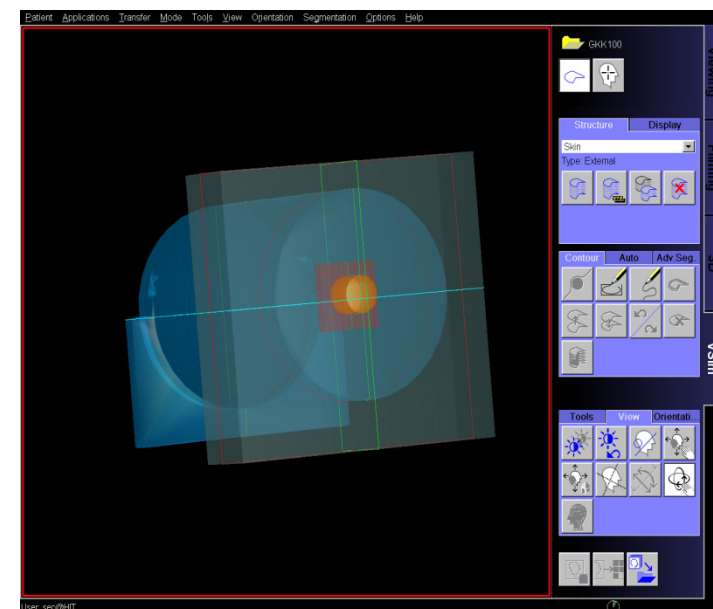


- edit existing structures in segmentation mode
 - use the ellipse or rectangle tool under the contour menu (switch between the two with right mouse click)
 - the ruler helps measuring the dimensions of your structure

- structures can be expanded to the previous/next slice by clicking on the corresponding button in the contour menu
- double click on an image will enlarge/close it
- the view menu offers zooming and rotation possibilities



- setting laser origin and ZP (Zielpunkt) in reference manager
 - attention: the ZP can only be set once!
- the result should look similar to screenshot 2 (depending on your geometry);
target in red, skin in gray and PMMA in both light blue and orange:



screenshot 2: Siemens patient system (contouring)

- save screenshots (“Drucken” on keyboard) as .png files using paint
- close patient with the bottom right button
- press “, Entf” on the keyboard to open the patient browser again
- send files to the HIT archive:
 - transfer -> send to -> HIT_ARCHIV
 - if your patient already exists in the archive simply sync and release lock

IMPORTANT: Always select the complete folder when sending files to the HIT archive;

check whether all files have been transferred



sync and release lock:

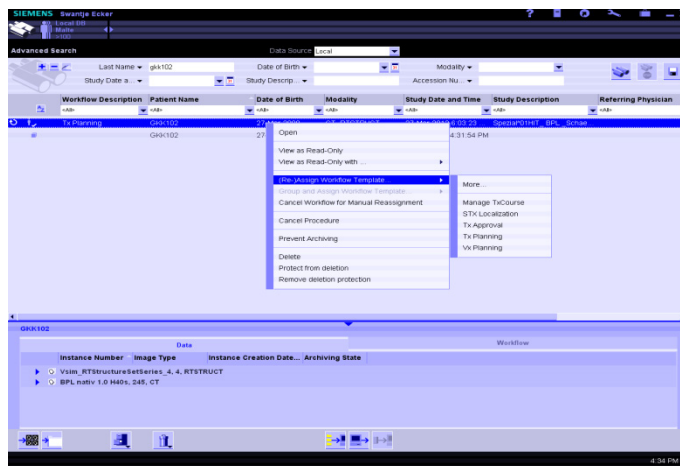


transfer status:

- switch to TPC in order to set up a treatment plan under

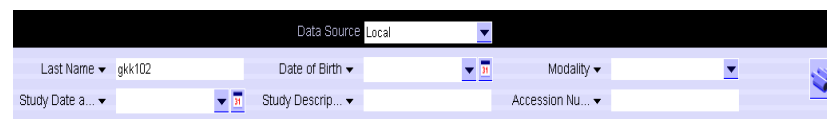
C.2.2 Treatment planning under Tx


- start the syngo.via software and enter a valid user name and password



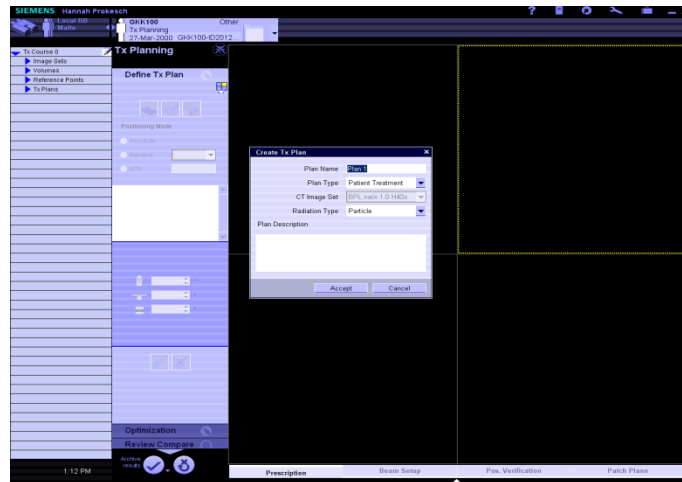
screenshot 3: syngo.via startup window

- select “HIT_ARCHIV” as data source and search the patient you want to create a treatment plan for with the goggles button on the right



- select the CT, RTSTRUCT-file and import it to the local database pressing:
 
 the bag (top right) will show you the importing process
- switch data source back to “Local” and re-search your patient by clicking on the goggles
- before you can open the CT, RTSTRUCT-file you always have to assign a workflow template:

- right click on CT, RTSTRUCT-file -> (re-)assign workflow template... -> Tx planning (see screenshot 3)
- a double click on the CT, RTSTRUCT-file to open







screenshot 4: define Tx plan

- define Tx plan:
 - to create a new Tx plan click on:
 - enter a plan name; plan type: patient treatment; CT image set: BPL native 1.0 H40s; radiation type: particle; plan description: optional
 - click on accept
 - four submenus will open: prescription, beam setup, pos. verification and patch plan
 - PRESCRIPTION:
 - number of fractions (Fx): 10 (in order to have the possibility of more than one radiation with the same treatment plan)



- dose type: effective in Gy
- prescription description: "10 x 1 Gy phys. Protonen" (depending on your desired particle type and dose)
- select the contoured target with prescription set to "MEDIAN"
- delete the max. dose und additional information





Prescription		Beam Setup		Pos. Verification		Patch Plane	
Number of Fx		10		Dose Type		<input type="radio"/> Absorbed in Gy	
						<input checked="" type="radio"/> Effective in GyE	
Prescription Description		10 x 1 Gy phys. Protonen					
Targets							
Type	Volume / Point	Prescr. Dose in GyE	Dose /Fx in GyE	Prescr. To	Weight	Nom. Prior Dose in GyE	
 Target		10.00	1.00	MEDIAN	1.00		
							
							
							

screenshot 5: prescription

Prescription		Beam Setup		Pos. Verification		Patch Plane						
Treatment Room		Room1		Patient Support		Room1Table						
Gating Support				Body Region								
Beam List												
Name	Targets	Energy	Fixed BL in °	Table (iso) in °	MLC in °	lat_je in cm	long_je in cm	vert_je in cm				
01T270	Target		90.0	270.0	0.0	0.00	0.00	0.00				
01T270- Details												
Weight		1.00		<div><div>Lateral Beamspot Density</div><div>FWHM in mm8.0</div><div>Grid Size in mm3.0</div><div>Longitudinal Beamspot Density</div><div>Ripple FilterNone</div><div>Bragg Peak Width in mm0.0</div><div>Range Step in mm2.0</div><div>Misc</div><div>Range Shifter</div></div>								
Tolerance Table		T11										
Table: Pitch		0.0 °							Roll		0.0 °	
Description												

screenshot 6: beam setup

○ BEAM SETUP:

- create a new Tx beam by clicking on: 
- name: 01T270; particle type: protons; fixed BL: 90°, table: 270°
- treatment room: Room1
- patient support: room1table
- assign ZP (Zielpunkt) as reference point in submenu; all positioning coordinates should switch to 0.00 
- lateral beam spot density: FWHM (8.0 mm) and grid size (3.0 mm); fixed settings for protons which should not be changed for optimization
- longitudinal beam spot density: ripple filter (none), Bragg peak width (0.0 mm) and range step (2.0 mm) (ignore warning message); The range step determines the energy settings. For protons a min. value of 1.0 mm is possible. The smaller the range step, the longer the total radiation time.
- weight: 1.00 (because there only is one beam)
- tolerance table: Tt1

Prescription		Beam Setup		Pos. Verification		Patch Plane	
Position Verification Groups							
Name	Tx Room	Tolerance Table	Organ Program	lat_iec in cm	long_iec in cm	vert_iec in cm	
<input checked="" type="checkbox"/> PV0	Room1	Tt1	AXKopt_...	0.00	0.00	0.00	▼
<input checked="" type="checkbox"/> 01T270_PV	Room1	Tt1	AXKopt_...	0.00	0.00	0.00	▼
<input type="checkbox"/>		▼	▼	▼			▼
<input type="checkbox"/>		▼	▼	▼			▼
<input type="checkbox"/>		▼	▼	▼			▼
<input type="checkbox"/>		▼	▼	▼			▼
Position Verification Beams							
Name	Imager Angles in °		Isocentric	Table Angles in °			
	Orbital	Angular		Isocentric	Pitch	Roll	
PV0_01	180.0	0.0	90.0	270.0	0.0	0.0	
PV0_02	270.0	0.0	90.0	270.0	0.0	0.0	

screenshot 7:

position verification

○ POSITION VERIFICATION:

- check both PV0 and 01T270_PV in order to active x-ray positioning
- Tx Room: Room1
- tolerance table: Tt1
- organ program: AXKopf_H1
- positioning parameters (lat_iec, long_iec, vert_iec) should automatically be set to 0.00

○ PATCH PLANE: no further settings necessary

- The Tx plan is now defined. Open the optimization menu:

Optimization 

- You will once again find four subtopics: dose constraints, beam weights, algorithm parameters and basic data set. The following settings are advised for a standard proton radiation plan.

- DOSE CONSTRAINTS:

- select “proton absorbed compound algorithm” as optimization technique



- min. target dose: 10 Gy (weight 1.00)
 - max. target dose: 10 Gy (weight: 2.00)
 - comment: Min. and max. dose are given for all fractions in total. The upper weight ratio states that the dose should rather be underestimated than overestimated.

- BEAM WEIGHTS: set to 1.00 because we created one beam

Dose constraints		Beam weights		Algorithm param.		Basic data set	
Dose calculation				Dose optimization			
	intermediate	final					
Dose grid resolution in mm	2.0	2.0		Number of iterations	50		
Double-Gaussian beam model	<input checked="" type="checkbox"/>	<input checked="" type="checkbox"/>		Objective function goal	0.001		
Scattering simulation	<input checked="" type="checkbox"/>	<input checked="" type="checkbox"/>		Optimization Strategy	SingleBeamOptimization		
Lateral cutoff in σ	3.5	3.5		Minimum ion count	500000		
Constant RBE factor	1.1			Regularization weight	0		
				Constr. weight normalization	<input type="checkbox"/>		
					lateral	proximal	distal
				Virt. target expansion in mm	3.0	0.0	2.0

screenshot 8:

algorithm parameters


- ALGORITHM PARAMETERS:

- dose grid resolution: 2.0 mm (intermediate) x 2.0 mm (final)
 - check double-Gaussian beam model for both intermediate and final
 - check scattering simulation for both intermediate and final
 - lateral cutoff in sigma:: 3.5 (intermediate) x 3.5 (final)
 - constant RBE factor: 1.1
 - number of iterations: appr. 50
 - objective function goal: 0.001
 - optimization strategy: SingleBeamOptimization
 - minimum ion count: 500000
 - regularization weight: 0
 - un-check constr. weight normalization
 - virtual target expansion: 3.0 mm (lateral) x 0.0 mm (proximal) x 2.0 mm (distal)
 - comment: The virtual target expansion gives additional degrees of freedom to the optimization routine. A broad virtual target allows scan spots outside the target volume. In order to improve the distal edge one can change the distal expansion to 1.0 mm

- You can now optimize your treatment plan:

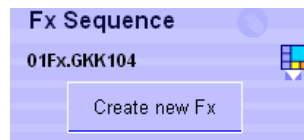


- If you are working with FNTDs and you want the protons to stop in the detector volume, we advise to have the 10% dose line at the end of the detector.

- The true absorbed dose will be optimized although the radiation can only be applied for calculated effective dose distributions. Therefore, a finalization under “proton effective compound algorithm” is necessary. Now, the dose distribution for the complete skin will be calculated which might significantly differ from the optimized absorbed dose distribution. The maximal dose changes to $RBE * 10 \text{ Gy} = 11 \text{ Gy}$.
- Start the finalization process with: 
- Close the patient and save your results with:



- An additional sync with the HIT archive is not required.
- If you have successfully created a Tx plan you finally need to approve it. (Re-)assign Tx approval as workflow template. You will be informed that all intermediate results will be discarded. Click on yes and continue the approval process:
 - FX SEQUENCE:
 - create new Fx (name: 01Fx.PatientName with 1 fraction per day)
 - highlight the plan and add it to Fx







create new Fx:



add plan to Fx:

- continue with REPORT APPROVE:



- report: report_minimal
- select the following content: patient information, Fx sequence information, MPR images, DVH of VOI (both VOI used in optimization and add all other VOI); attention: always wait for software to attach the desired information! 
- toggle relative 3D distribution: 
- color iso-dose areas: 
- manually set dose to 10.0 Gy and select 5 iso-dose lines: (10%, 50%, 70%, 90%, 107%) 
- image set: BPL nativ 1.0 H40s
- add additional images (optional)

- create report and approve (password required) and save the pdf-file
- send to treatment
- archive results

Tx Approval

Fx Sequence
Review Compare
Report Approve

01Fx.GKK101

Review

GKK101 eff

Beam Dose Selection

01T270

Image Set

BPL nativ 1.0 H40s

Create Report & Approve
Unapprove
Send To Treatment
Send To Planning

GKK101
GKK101-ID20120327
*27-Mar-2000, 0, 12Y

GKK101_REL
Effective
Relative

A

100.00 %
50.00 %
75.00 %
90.00 %
107.50 %

100% = 10.00 GyE
Loc = 5.86 GyE
Glob = 11.42 GyE

GKK101
GKK101-ID20120327
*27-Mar-2000, 0, 12Y

H

100.00 %
50.00 %
75.00 %
90.00 %
107.50 %

100% = 10.00 GyE
Loc = 11.16 GyE
Glob = 11.42 GyE

GKK101
GKK101-ID20120327
*27-Mar-2000, 0, 12Y

H

100.00 %
50.00 %
75.00 %
90.00 %
107.50 %

100% = 10.00 GyE
Loc = 11.16 GyE
Glob = 11.42 GyE

01Fx.GKK101-Report

Contents

Report Report_Minimal

Attachment

Add Selected Image
Add All Images
Delete Image

General

Patient information ☒
Fx Sequence information ☒

Per Plan

MPR images (3 orthogonal + manually Added) ☒
Textual information(All beams,inc PVD,PV Beam) ☐
Basic STXInformation ☐
DVH of VOI ☒
VOI used in Optimization ☒
Add all other VOI ☒

Fx Sequence

DVH of VOI ☐
VOI used in Optimization ☐
Add all other VOI ☐
MPR images (3 orthogonal + manually Added) ☐

01Fx.GKK101-Report

A

100.00 %
50.00 %
75.00 %
90.00 %
107.50 %

100% = 10.00 GyE
Loc = 5.86 GyE
Glob = 11.42 GyE

H

100.00 %
50.00 %
75.00 %
90.00 %
107.50 %

100% = 10.00 GyE
Loc = 11.16 GyE
Glob = 11.42 GyE

GKK101
GKK101-ID20120327
*27-Mar-2000, 0, 12Y

GKK101_REL
Effective
Relative

100.00 %
50.00 %
75.00 %
90.00 %
107.50 %

100% = 10.00 GyE
Loc = 11.16 GyE
Glob = 11.42 GyE

screenshot 9: report approve

D BIBLIOGRAPHY

- [1] G.M. Akselrod, M.S. Akselrod, E.R. Benton and N. Yasuda: A novel Al_2O_3 fluorescent nuclear track detector for heavy charged particles and neutrons. *Nuclear Instruments and Methods in Physics Research, B* 247, pp. 295–306 (2006).
- [2] M.S. Akselrod, A.E. Akselrod, S.S. Orlov, S. Sanyal and T.H. Underwood: Fluorescent Aluminum Oxide Crystals for Volumetric Optical Data Storage and Imaging Applications. *Journal of Fluorescence*, Vol. 13, No. 6, pp. 503–511 (2003).
- [3] M.S. Akselrod and G.J. Sykora: Fluorescent nuclear track detector technology – A new way to do passive solid state dosimetry. *Radiation Measurements*, Vol. 46, pp. 1671–1679 (2011).
- [4] M.S. Akselrod, R.C. Yoder and G.M. Akselrod: Confocal fluorescent imaging of tracks from heavy charged particles utilising new Al_2O_3 : C, Mg crystals. *Radiation Protection Dosimetry*, Vol. 119, No. 1–4, pp. 357–362 (2006).
- [5] Carl Zeiss MicroImaging GmbH: LSM 710 – The Power of Sensitivity. URL: <http://www.zeiss.de/sensitivity> (2009).
- [6] A. Fassò, A. Ferrari, J. Ranft and Paola Sala: FLUKA. URL: https://www.fluka.org/fluka.php?id=secured_intro. Advanced Interface (flair) by V. Vlachoudis (version 0.9-7 [R1593]) (2012).
- [7] Gammex Inc.: Tissue Characterization Phantom 467 Data Sheet. URL: http://www.gammex.com/ace-images/RO_467.pdf (2012).
- [8] S. Greulich, J.-M. Osinga, M. Niklas, F.M. Lauer, J.A. Bartz, M.S. Akselrod and O. Jäkel: Quantative read-out of Al_2O_3 : C, Mg-based fluorescent nuclear track detectors using a commercial confocal microscope. *in prep.*
- [9] Heidelberg University Hospital: Ion beam irradiation – unparalleled precision and effectiveness. URL: <http://www.klinikum.uni-heidelberg.de/index.php?id=116993&L=1> (2012).
- [10] N. Hünemohr: Improvement of ion therapy planning by use of dual energy computed tomography. Diploma thesis at the University of Heidelberg and the German Cancer Research Center (2011).
- [11] ICRU: Fundamental Quantities and Units for Ionizing Radiation. *International Commission on Radiation Units and Measurements*, Report 60 (1998).

- [12] F. Lauer: Investigations of a fluorescent nuclear track detector for use in therapeutic ion beams. Diploma thesis at the University of Heidelberg and the German Cancer Research Center (2011). Scanning. URL: <http://www.medimagingsales.com/images/general-systems/ct/siemens/siemens-sensation-4/Siemens-Somatom-Sensation-4-CT-Brochure.pdf> (2011).
- [13] Max Planck Institute for Nuclear Physics: The Heidelberg Ion Beam Facilities. URL: <http://www.mpi-hd.mpg.de/blaum/accelerators/index.en.html> (2012).
- [14] Mint Medical: MITK 3M3 Image Analysis. URL: <http://www.mint-medical.de/productssolutions/mitk3m3/mitk3m3/> (2012).
- [15] P. Nanda: Stack profile Plot. URL: <https://gist.github.com/2029530> (2011).
- [16] R Development Core Team: The R Project for Statistical Computing. URL: <http://cran.r-project.org/bin/windows/base/> (version 2.15.0) (2012).
- [17] W. Rasband: ImageJ. URL: <http://rsbweb.nih.gov/ij/> (2012).
- [18] Siemens AG Medical Solutions: SOMATOM Sensation 4 – Computed Tomography System for Multislice Spiral Scanning. URL: <http://www.medimagingsales.com/images/general-systems/ct/siemens/siemens-sensation-4/Siemens-Somatom-Sensation-4-CT-Brochure.pdf> (2011).
- [19] G.J. Sykora and M.S. Akselrod: Novel fluorescent nuclear track detector technology for mixed neutron-gamma fields. *Radiation Measurements*, Vol. 45, pp. 594–598 (2010).
- [20] G.J. Sykora and M.S. Akselrod: Photoluminescence study of photochromically and radiochromically transformed Al_2O_3 : C, Mg crystals used for fluorescent nuclear track detectors. *Radiation Measurements*, Vol. 45, pp. 631–634 (2010).
- [21] G.J. Sykora, M. Salasky and M.S. Akselrod: Properties of novel fluorescent nuclear track detectors for use in passive neutron dosimetry. *Radiation Measurements*, Vol. 43, pp. 1017–1023 (2008).
- [22] J.F. Ziegler, J.P. Biersack and M.D. Ziegler: SRIM – The Stopping and Range of Ions in Matter. URL: <http://www.srim.org/SRIM/SRIMLEGL.htm> (version 2012.01) (2012).

ACKNOWLEDGMENTS

I would like express my gratitude to Prof. Dr. Wolfgang Schlegel, head of the Department of Medical Physics in Radiation Oncology at the German Cancer Research Center (DKFZ), for giving me the opportunity to work in his research division. I would like to thank Prof. Dr. Oliver Jäkel for accepting me in his research group and introducing me to the field of academic work. Furthermore, I want to thank Prof. Dr. Uwe Oelfke for drawing my interest to medical physics with unique lectures and for being the second referee of this thesis and the representative of the Department of Physics and Astronomy.

A special thanks goes to Dr. Steffen Greulich. Writing this thesis would not have been possible without his outstanding support and tremendous dedication. His advice and guidance has always been deeply appreciated. I would like to thank the Heavy Ion Therapy Research Group for a great work atmosphere and fruitful discussions on lunch and coffee breaks. I am thankful to Christoph Tremmel for measuring the WEPLs of PMMA and aluminum oxide and to Julia-Maria Osinga and Nora Hünemohr for company and support on irradiation and readout days.

Furthermore, I would like to thank Dr. Mark S. Akselrod from Landauer Inc. for supplying us with FNTDs and Dr. Felix Bestvater from the DKFZ light microscopy facility for readout times. I would also like to thank Dr. Roland Repnow and Manfred König from the Operations and Maintenance Group at MPI-K for precise und uncomplicated FNTD irradiation as well as Dr. Michael Holzscheiter for putting us into contact with them.

Another thanks goes to Dr. Stephan Brons, Dr. Peter Heeg and Benjamin Ackermann from HIT for technical advisory and support during irradiations. I would especially like to thank Swantje Ecker for her patience and time explaining the patient treatment software. Contouring and planning would have been very time-consuming without her knowledge and help.

Last but not least, I would like thank my family and friends for always finding ways to take my focus off work from time to time. I am thankful to Tess Thurber for polishing up my rusty English and spotting numerous mistakes. My wonderful sisters and parents provided me with a very different view on the subject over the past three months. Their unconditional belief and encouragement will not be forgotten.

Assurance

I hereby confirm that I have written this thesis independently and that I have not used any other than the specified sources.

Heidelberg, 24th May 2012

Erklärung

Ich versichere, dass ich diese Arbeit selbstständig verfasst und keine anderen als die angegebenen Quellen und Hilfsmittel benutzt habe.

Heidelberg, den 24. Mai 2012

.....

